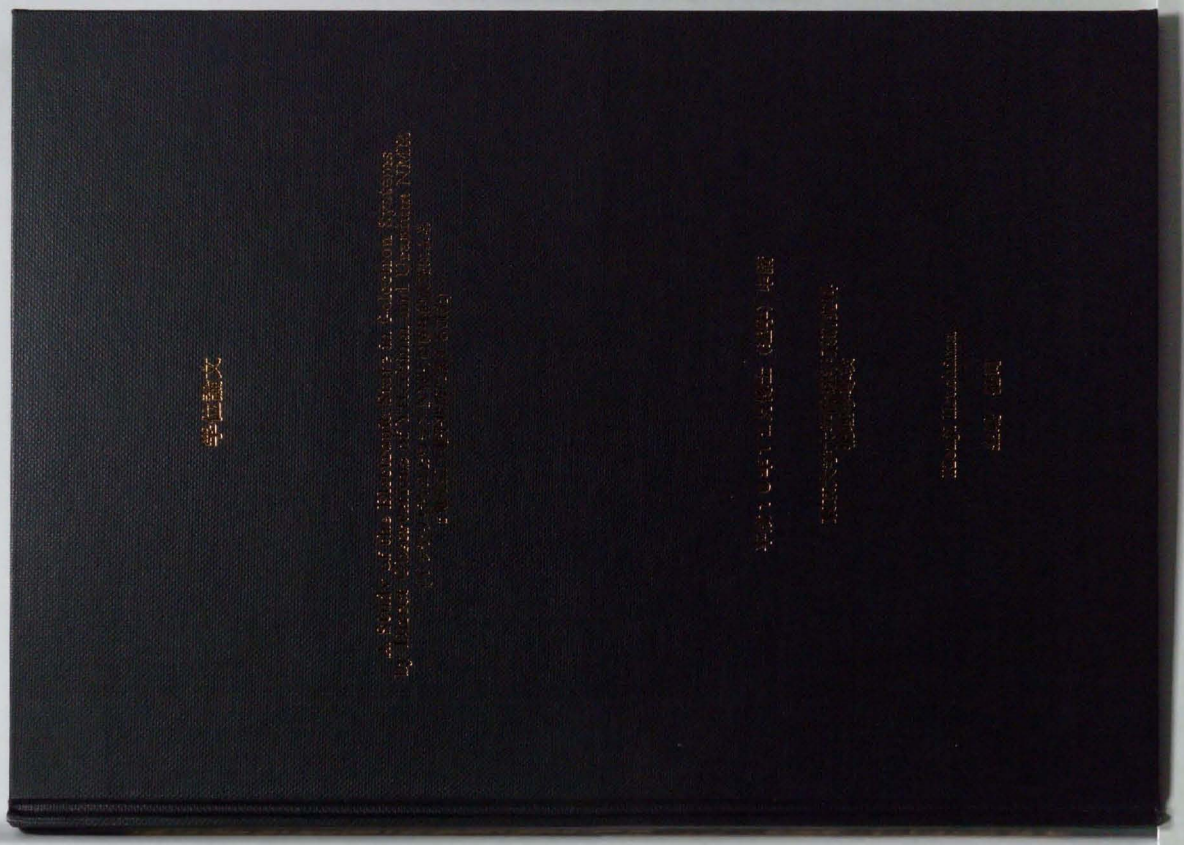

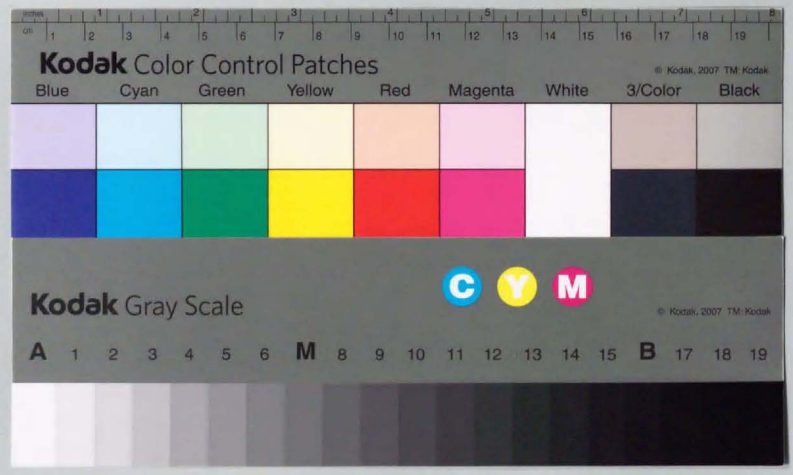
Kodak Color Control Patches
© Kodak, 2007 TM: Kodak
Blue
Cyan
Green
Yellow
Red
Magenta
White
3/Color
Black
Kodak Gray Scale
C
Y
M
© Kodak, 2007 TM: Kodak
A 1 2 3 4 5 6 M 8 9 10 11 12 13 14 15 B 17 18 19

学位論文

A Study of the Electronic State in f-electron Systems by Direct Observations of Ytterbium and Uranium NMR

(イッテリビウムとウランNMRの直接的観測による
f電子系の電子状態に関する研究)

平成１０年１２月博士（理学）申請

東京大学大学院理学系研究科
物理学専攻

Kenji Ikushima

生嶋　健司

Acknowledgments

First of all, I would like to express my sincere thanks to Professor H. Yasuoka for his suggestion of the problem and his stimulating help and guidance during the research. I also wish to thank Professor M. Takigawa for his interest and helpful discussions.

I am grateful to Professor Y. Ueda, and the members in his laboratory for their assistance of measurements of the susceptibility and the useful suggestions.

Thanks are also due to my colleagues, Dr. T. Ohama, Dr. Y. Itoh, Dr. J. Kikuchi, Dr. A. Goto, Dr. N. Fujiwara, Mr. Y. Ueda, Mr. S. Fujiyama, Mr. K. Nakayama and Mr. Y. Kato for their enlightening suggestions and stimulating discussions. Dr. J. Kikuchi especially taught me the experimental techniques of the nuclear magnetic resonance in my early days in Professor Yasuoka's laboratory.

Next, I wish to thank Professor F. Iga, Mr. N. Shimizu and Professor T. Takabatake for their high quality samples. I am also grateful to Mr. S. Tsutusi, Mr. N. Masaki, Dr. A. Nakamura for their assistance of experiments at Japan Atomic Energy Research Institute (JAERI) as well as their carefully prepared sample. In addition, I wish to thank Professor S. Nasu, Professor M. Date and Dr. M. Saeki for giving opportunity for the uranium NMR experiments at JAERI.

I would finally like to my mother, father and especially my wife, Mari, whose interest, help and continued encouragement were instrumental in insuring the completion of this work.

Contents

Chapter 1

Introduction

1.1 f-electron Systems

In the "normal" compound, the rare earth ions and the heavy actinide ions are in trivalent state and most of them order magnetically at low temperatures, whereas the light actinide ions like uranium ions are of an open question about the valence in solids, except for some special cases such as the tetravalent state of UO_2 or the trivalent state of UPd_3. In the light actinides the 5f-electrons are described frequently as itinerant, and paramagnetic, magnetic with a small moment or even superconducting ground states are favored. Certain rare earth compounds, especially those based on Ce, Sm, Eu, Tm, Yb, are non-magnetic metals or non-magnetic semiconductors in the ground state. These systems also exhibit a variety of unusual magnetic, thermodynamic and transport properties. The anomalous behavior is driven by a second ionic configuration, which in solids has an energy comparable to the trivalent one. The ionic configuration leading to a valence instability of the f-shell is the divalent one for Sm, Eu, Tm, Yb and the tetravalent one for Ce. In part as a consequence of the valence instability these systems have a relatively large hybridization between the f-states and the conduction band states. The hybridization allows the f-electrons to delocalize to some extent, including fluctuations in the f-charge, as well as in the spin and orbital degrees of freedom. This mechanism is capable of preventing magnetic order and will give rise to mixed-valent and heavy fermion behavior.

In this section, we briefly introduce the physical properties of the ytterbium dodecaboride (YbB_{12}) and the uranium dioxide (UO_2) in which we succeeded in direct observation of magnetic on-site NMR. The former is one of several compounds with a small gap in their excitation spectrum, the so-called "Kondo semiconductor" or "Kondo Insulator"[1], and the latter is a typical system of the localized tetravalent state of which the ground state is the coexistence of the antiferromagnetic and the antiferroquadrupole ordering.

1.1.1 Kondo Semiconductor, YbB_{12}

The systems classified as the Kondo semiconductors have been discovered in several rare earth-based compounds. The classical examples are SmB_6[2] and YbB_{12}[3] with cubic crystal structure [Fig. 1.1], and the relatively resent examples are Ce-based compounds

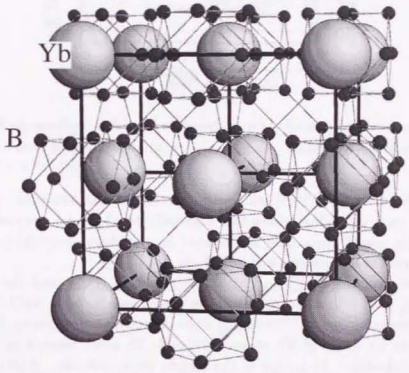

Figure 1.1: The crystal structure of YbB_{12}.

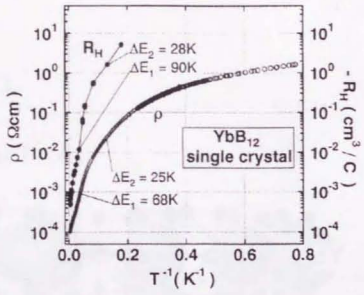

Figure 1.2: Temperature dependence of electric resistivity ρ and Hall coefficient R_H for a single crystal sample of YbB_{12}. (From Ref. [8])

such as CeNiSn[4] or CeRhSb[5] with orthorhombic crystal structure. Although these systems have each individual character, especially by the local symmetry at the rare earth sites, the overall discussion is reported on the short review[1] and macroscopic experimental results are summarized in Ref. [6].

The crystal structure of YbB_{12} has an fcc structure ($D2_f$), and the space group is $Fm3m$-O_h^5 [Fig. 1.1]. This structure can be considered to be a NaCl-type, where Na and Cl are corresponding to Yb and B_{12} cubo-octahedra, respectively, but can be also described as an fcc array of Yb atoms with each Yb atom located in the center of a $(B_4)_6$ cubo-octahedron. In groups of the Kondo semiconductors, YbB_{12} shows a clear gap formation in transport properties [Fig. 1.2] and magnetic susceptibility χ [Fig. 1.3]. At high temperatures the values of electric resistivity are of the same order as that in typical Kondo lattice systems like $CeCu_6$, whereas below about 50 K it exponentially increases as temperature (T) decreases. Assuming a single carrier model, the number of conduction electrons is estimated to be about one per unit cell at room temperature, but it drastically decreases as T decreases and reaches to the value of about 7.4×10^{-6} per unit cell at 1.7 K[7]. As seen in Fig. 1.2, the activation energy Δ seems to be dependent on T, and this suggests that the origin of the energy gap is different from that of usual semiconductors. The presence of the excitation gap in YbB_{12} can be further established by the measurements of the ^{11}B nuclear spin-lattice relaxation rate, $1/T_1$[7]. In Fig. 1.4, we see the rapid reduction below 80 K due to the energy gap, whereas the up-turn below 15 K remained to be not clarified.

The magnetic susceptibility has a pronounced peak at about 80 K, and then rapidly

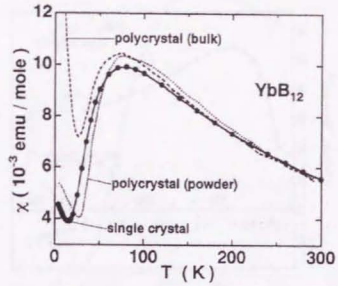

Figure 1.3: Temperature dependence of magnetic susceptibility χ for single crystal and polycrystal samples of YbB_{12}. (From Ref. [8])

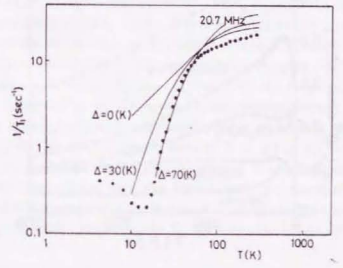

Figure 1.4: Temperature dependence of the ^{11}B nuclear spin-lattice relaxation rate in YbB_{12}. (From Ref. [7])

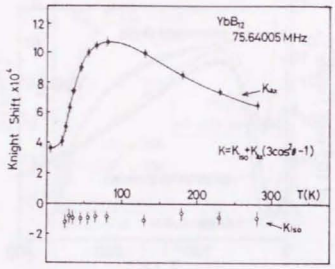

Figure 1.5: Temperature dependence of the Knight shift at the ^{11}B sites in YbB_{12}. (From Ref. [7])

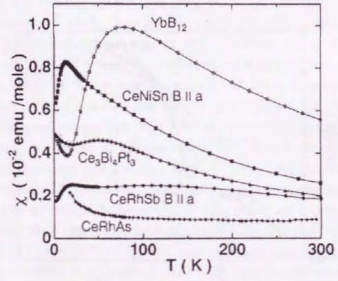

Figure 1.6: Temperature dependence of the magnetic susceptibility in the Ce and Yb-based Kondo semiconductors. (From Ref. [6])

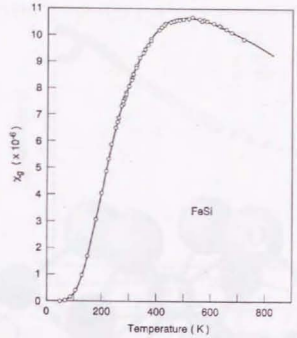

Figure 1.7: Temperature dependence of the magnetic susceptibility of FeSi. (From Ref. [9])

decreases as T decreases. The effective moment is estimated to be 4.09 μ_B above 170 K, which is almost corresponding to the effective moment of Yb^{3+}, 4.54 μ_B. Although the susceptibility has a sample dependence at low temperatures, the intrinsic T-dependence, which is constant at $T \ll \Delta$, is confirmed by the T-dependence of the Knight shift in the ^{11}B NMR experiments[7] [Fig. 1.5]. It is worthy of notice that the Curie term at low temperatures in the resent high quality single crystal[8] is rather smaller than that of the powdered sample. Nevertheless, the susceptibility roughly half the maximum value around 80 K remains at $T \to 0$. As seen in Fig. 1.6, this large susceptibility remained at $T \to 0$ is also observed in all Ce-based Kondo semiconductors[6]. In contrast, the susceptibility of a transition metal compounds, FeSi, which is a similar semiconductor with an energy gap of 170 K[9], is nearly zero at $T \to 0$[Fig. 1.7]. Considering that the reduction of the susceptibility due to the energy gap is only effective for the spin part associated with electronic states near the Fermi level, the susceptibility for rare earth-based semiconductors remained at $T \to 0$ should be attributed to the extremely large Van Vleck type contribution[10]. Experimentally, however, the origin of this susceptibility is not clarified.

1.1.2 Antiferromagnet, UO_2

Uranium dioxide is an ionically-bounded semiconductor with two 5f electrons on each

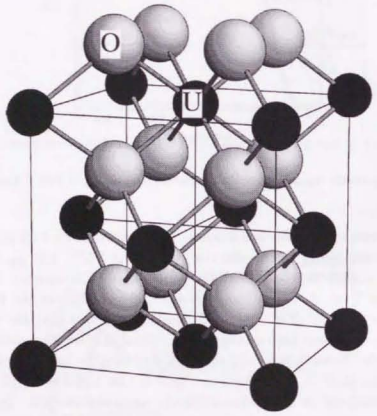

Figure 1.8: The crystal structure of UO_2.

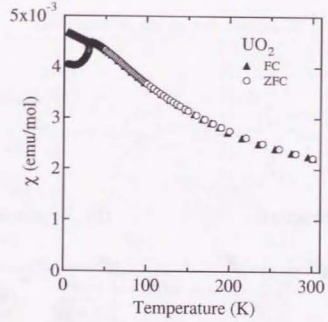

Figure 1.9: Temperature dependence of the magnetic susceptibility of UO_2.

U^{4+} ion. The Hund's rule ground state is $^3H_4$. The crystal structure of UO_2 is the face-centered-cubic fluorite structure as illustrated in Fig. 1.8. In the presence of a cubic crystalline field, the ninefold degeneracy of the $^3H_4$ state is reduced to triplet Γ_5 and Γ_4 states, a doublet Γ_3 and a singlet Γ_1. Rahman *et.al.* diagonalized the complete Hamiltonian for UO_2 including Coulomb, spin-orbit and crystal-field terms [11]. They found the Γ_5 triplet state separated by 170 meV from a first-excited Γ_3 states. Experiments at the pulsed neutron source give an evidence for such an excitation at 161 meV[12].

The degeneracy of the ground state of a system of ions with an even number of electrons can be lifted by the transition to a magnetically ordered state or by the Jahn-Teller transition involving a distortion of a lattice. Uranium dioxide is a striking example of the system where the exchange interactions and the Jahn-Teller interaction via the phonons are comparable in size.

The antiferromagnetic transition at T_N =30.8 $\pm$ 0.3 K is of the first order phase change[13]. The magnetic susceptibility is shown in Fig. 1.9. The effective moment is estimated to be about $3.0\mu_B$, which is somewhat larger than that of the Γ_5 ground state, $2.83\mu_B$, and is smaller than that of the $^3H_4$ state, $3.58\mu_B$. Uranium dioxide has the type-I antiferromagnetic structure in which there are (001) ferromagnetic planes stacked in an alternating plus minus sequence[13]. In a multi-domain crystal, the spin directions cannot be determined by the neutron diffraction, but they were known to lie in the $\langle 110 \rangle$ directions. The neutron diffraction experiments by Faber and Lander[14] proposed a non-collinear $2k$ structure with the spins alternating between [110] and [$\bar{1}$10] directions. They found a small shift (0.014 Å) of the oxygen atoms from their equilibrium position with

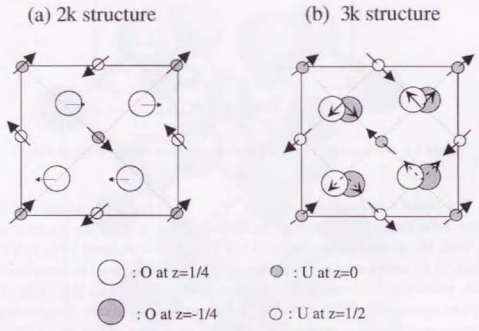

Figure 1.10: The (001) projection of the fluorite structure to display the double-$\boldsymbol{k}$ and triple-$\boldsymbol{k}$ structures which are possible in UO_2[17]. In the double-$\boldsymbol{k}$ structure the displacements are along ⟨010⟩, whereas in the triple-$\boldsymbol{k}$ structure they occur along ⟨111⟩; dashed and closed arrows are for down and up displacements. In a double-$\boldsymbol{k}$ structure the magic moments lie along ⟨110⟩ whereas in a triple-$\boldsymbol{k}$ structure they are along ⟨111⟩.

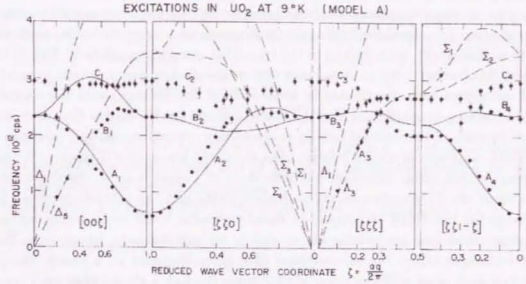

Figure 1.11: Magnon-phonon coupled dispersion relations for UO_2 measured by Cowey and Dolling[15]. The phonons at room temperature are shown as broken lines.

no change in the unit cell dimensions. The magnetic excitations in the antiferromagnetic state were measured by Cowley and Dolling[15] who found the first example of the interaction between magnons and phonons.

The theory of UO_2 by Allen[16] gives a satisfactory explanation of the first-order phase transition through the spin-lattice interaction which is an interplay between the exchange and the quadrupole coupling. The physical mechanism for the quadrupole coupling is the modification of the crystalline field acting on the 5f electrons by the motion of surrounding O^{2-} ions. The theory shows how the quadrupole coupling manifests itself in the behavior of the C_{44} elastic constants above the ordering temperature. As the result of the dynamic coupling between uranium quadrupoles and oxygen atom displacements, the observed ultrasonic velocity is renormalized by the quadrupole response. The theory also gives a good account of the two branches of spin-waves observed in the neutron scattering experiments.

In Allen's model the spins lie in ⟨110⟩ directions. However, Allen assumed that they were all parallel to a single [110] direction, whereas in the model of Faber and Lander[14] they occupy all four ⟨110⟩ directions within an (001) plane, so-called the $2\boldsymbol{k}$-structure in Fig. 1.10(a). In addition, as a result of a careful analysis of the possible magnetic structures, it is pointed out that the $3\boldsymbol{k}$-structure with the $3\boldsymbol{k}$ crystallographic distortion also minimize the quadrupole energy as well as the exchange energy [18, 17] [Fig. 1.10(b)].

1.2 Studies of f-electron Systems by NMR/NQR Techniques

The nuclear magnetic resonance (NMR) techniques have provided us with fruitful results on the studies of the local electronic state in magnetic and superconducting materials for a long time. Especially, with respect to the transition metal compounds as High T_c cuprates in which 3d-electrons play an important role on the electric and magnetic properties, the NMR techniques have contributed to acquisition of information about the magnetic and superconducting properties. From the NMR spectra we can clarify the static magnetic properties such as the internal field in magnetically ordered states, and from the nuclear relaxation rates we can obtain informations about the low energy magnetic excitation. In addition, we can often determine the spin state of Cooper pair in the superconducting states from the T-dependences of the Knight shifts and the relaxation rates. Such an advantage for the NMR techniques is mainly because NMR experiments for magnetic transition metal ions are practicable as well as for non-magnetic ligand ions. Since the NMR technique utilize nuclei composed of a given material as a probe, the physical quantities associated with the electrons are given through a short-range weak interaction between the nucleus and electrons, that is hyperfine interaction. Thus we often need to know the magnitude and the mechanism of the hyperfine interaction to obtain information about the electronic states around the probed nucleus. This means that the NMR at the magnetic sites is more advantageous to investigation of magnetic properties in a given material than at the non-magnetic sites. Furthermore, the mechanism of the hyperfine field at the magnetic sites is clearer than that at the non-magnetic ligand site except for the classical dipole-dipole interaction. In Sec. 1.2.1, we will describe the analyses in non-magnetic ligand NMR, which is a usual method in f-electron systems. In Sec. 1.2.2, we will explain the hyperfine field at the rare earth and actinide sites and restriction of observation of rare earth and actinide NMR.

1.2.1 Approach from Non-magnetic Ligand NMR

The magnetic hyperfine interaction at the i-th site with the nuclear spin $\boldsymbol{I}_\mathrm{i}$ within a ground term (J, L, S) of f-electrons has the general form

$$\mathcal{H}_\mathrm{HFI} = \boldsymbol{I}_\mathrm{i} \cdot \sum_\mathrm{j} \tilde{A}_\mathrm{ij} \cdot \boldsymbol{J}_\mathrm{j}, \tag{1.1}$$

where $\tilde{A}_\mathrm{ij}$ and $\hbar\boldsymbol{J}_\mathrm{j}$ are the hyperfine tensor at the i-th site due to the j-th site, and an angular momentum at the j-th sites in LS coupling, respectively. The term with i=j represents on-site hyperfine interaction, and the term with $\mathrm{i} \neq \mathrm{j}$, which includes the classical dipole-dipole interaction and the transferred hyperfine interaction (THI), is due to surrounding ligand sites. For the magnetic rare earth and actinide NMR the on-site term $\tilde{A}_\mathrm{i=j}$ ($\sim 10^7$ Oe) is a major contribution, while for the non-magnetic ligand NMR the $\tilde{A}_\mathrm{i\neq j}$ term from the magnetic sites ($10^2 \sim 10^4$ Oe) is usually dominant and important to obtain information on the magnetic properties of f-electrons. This indicates that the non-magnetic ligand NMR is of advantage for the investigation of magnetic structure because

the hyperfine interaction is sensitive to the properties of surrounding magnetic sites. In this section, we introduce the typical analyses of the NMR results at the non-magnetic ligand sites. We rewrite the magnetic hyperfine interaction at non-magnetic ligand sites into the form of an interaction between the nuclear dipole moment $\boldsymbol{\mu}_\mathrm{N} = \gamma_\mathrm{N}\hbar\boldsymbol{I}$ and a magnetic local field $\mathbf{H}_\mathrm{loc}$ as follows,

$$\mathcal{H}_\mathrm{HFI} = -\boldsymbol{\mu}_\mathrm{N} \cdot \boldsymbol{H}_\mathrm{loc}, \tag{1.2}$$

$$\boldsymbol{H}_\mathrm{loc} = \boldsymbol{H}^\mathrm{MG}_\mathrm{thf} + \boldsymbol{H}^\mathrm{MG}_\mathrm{dip} + \boldsymbol{H}^\mathrm{NM}_\mathrm{onsite}, \tag{1.3}$$

where $\boldsymbol{H}^\mathrm{MG}_\mathrm{thf}$ and $\boldsymbol{H}^\mathrm{MG}_\mathrm{dip}$ are the transferred hyperfine field and the classical dipole field from the magnetic sites, respectively, and $\boldsymbol{H}^\mathrm{NM}_\mathrm{onsite}$ is the on-site contribution due to non-magnetic s or p-electrons around the nucleus.

We often assume the Knight shift in the applied field, H_0, as follows,

$$\begin{aligned} K(T) &= \frac{\langle H_\mathrm{loc}\rangle}{H_0} \\ &= \frac{A_\mathrm{f}}{N_\mathrm{A}\mu_\mathrm{B}}\chi_\mathrm{f}(T) + \frac{A^\mathrm{NM}_\mathrm{CE}}{N_\mathrm{A}\mu_\mathrm{B}}\chi^\mathrm{NM}_\mathrm{c} + \frac{A^\mathrm{NM}_\mathrm{orb}}{N_\mathrm{A}\mu_\mathrm{B}}\chi^\mathrm{NM}_\mathrm{orb} \\ &= K_\mathrm{f}(T) + K_\mathrm{CE} + K_\mathrm{orb}, \end{aligned} \tag{1.4}$$

where $\langle H_\mathrm{loc}\rangle$ is the time average of the local field at the nucleus, N_A is the Avogadoro's number, and χ and A represent the susceptibility and hyperfine coupling constant corresponding to the hyperfine field, respectively. In the NMR experiments, the value of A is usually given in the unit of $\mathrm{kOe}/\mu_\mathrm{B}$ or $\mathrm{T}/\mu_\mathrm{B}$. In these formula, the first term indicates the contribution due to f-electrons including the THI and the classical dipole-dipole interaction, and it shows the T-dependence corresponding to the susceptibility due to f-electrons, χ_f. The second and third terms indicate the spin part due to s or p-conduction electrons and the orbital part, respectively, and they are independent on T. The mechanism of THI in rare earth and actinide intermetallics is considered as a result of the exchange polarization of conduction electrons by f-electrons. Although the classical dipole field is easily calculated, the exact evaluation of THI is impossible because the detailed knowledge about the c-f mixing is requested for the analysis. Thus we experimentally obtain the hyperfine coupling constant, A_f, from the K vs χ plot with an implicit parameter T, and discuss the presence of the THI by comparing with the calculated classical dipole field. When the Knight shift is independent on T, it is difficult to investigate the physical origin of the Knight shift because the K vs χ plot is not applicable. This is a serious problem especially on the investigation of the Knight shift in the superconducting states or in the ground state of the Kondo semiconductors.

The fluctuating components of the local field, δH_loc, cause the relaxation phenomena of the nuclear magnetization. Let z be the direction of quantization for the nuclear and electronic spin systems. The general form of the nuclear spin-lattice relaxation rate, $1/T_1$, is then given by

$$\frac{1}{T_1} = \frac{\gamma_\mathrm{N}}{2}\int_{-\infty}^{+\infty} dt \langle\{\delta H^-_\mathrm{loc}(t)\delta H^+_\mathrm{loc}(0)\}\rangle \exp(-i\omega_\mathrm{n}t), \tag{1.5}$$

where $H^{\pm}_{\rm loc} = H^{x}_{\rm loc} \pm iH^{y}_{\rm loc}$, $\{AB\} = (AB + BA)/2$, and $\omega_{\rm N}$ is the NMR frequency. In eq. (1.5), the nuclear spin-lattice relaxation rate is just Fourier component at the NMR frequency of those elements of the fluctuating local field which are transverse to the quantization direction. Using the transverse Fourier component of the hyperfine coupling constant, $A_{\perp}(q)$, and the imaginary part of the transverse component of the dynamical susceptibility, $\chi''(q,\omega)$, we can also express the nuclear spin-lattice relaxation rate[19],

$$\frac{1}{T_1} = \frac{k_{\rm B}T\gamma_{\rm N}^2}{\mu_{\rm B}^2}\sum_{q} A_{\perp}^2(q)\ \chi''(q,\omega_{\rm N}), \tag{1.6}$$

where $k_{\rm B}$ is the Boltzmann's constant. For the normal metals like Na metal, it obeys the Korringa relation

$$\frac{K^2}{R} = \text{const.} \tag{1.7}$$

where $R = 1/(T_1T)$. In rare earth and actinide intermetallics, we often assume the similar form as the Knight shift:

$$R(T) = R_{\rm f}(T) + R_{\rm CE} + R_{\rm orb}. \tag{1.8}$$

The first term is usually much larger than the second term due to the conduction electrons. We often obtain the first term by subtracting the R in the non-magnetic reference material like La-based compounds from the measured values, but the analysis is not always applicable because the band structure in the reference material may quite different from the magnetic material near the Fermi level. If we can fortunately pick out the $R_{\rm f}$ from the experimental values, we get the convenient form

$$R_{\rm f} = \frac{2z\gamma_{\rm N}^2 k_{\rm B}}{\mu_{\rm B}^2}\left(\frac{A_{\rm f}}{z}\right)^2\chi_{\rm f}\frac{\tau_{\rm f}}{\hbar}, \tag{1.9}$$

where z and $\tau_{\rm f}$ are the number of the ligand magnetic sites and the correlation time of f-spins, respectively. Then we assume that the dynamical susceptibility has a Lorentzian form with the characteristic energy, $\Gamma(q) = \hbar/\tau_{\rm f}$,

$$\chi(q,\omega) = \frac{\chi(q)}{1 - i\omega/\Gamma(q)}, \tag{1.10}$$

and that the these q-dependences are neglected. These analytical processes are useful for investigation on the characteristic energy of f-electrons.

We should also note that the expression in eq. (1.8) is an approximation that fluctuations between local fields with different origins do not contribute to the relaxation processes. Particuraly, in the systems with the strong c-f mixing, validity of the expression in eq. (1.8) is not assured. We describe the feature for the non-magnetic ligand NMR as follows.

- We can precisely measure the NMR quantities (K or R) over a wide temperature region including the anisotropy of those. We can discuss qualitatively the T-dependence.

- The non-magnetic ligand NMR can sometimes determine the most possible magnetic structure among those proposed by the neutron scattering experiments, because the hyperfine interaction is due to the contribution from surrounding magnetic sites.
- It is difficult to discuss quantitatively the physical origin of the NMR quantities. Sometimes we cannot determine even whether they are reflected with the properties of f-electrons.

1.2.2 Approach from Magnetic Rare Earth and Actinide NMR

Unlike 3d ions, for which the orbital angular momentum is quenched, the dominant contributions to the hyperfine field at the rare earth and actinide nuclei in solids arise from the angular momentum (spin and orbital) of the f-electrons. This is of the order of 10^7 Oe. As the result, the contribution from the ligand sites is usually negligible. In the magnetic rare earth and actinide NMR, we can write the magnetic hyperfine interaction into a simple form (see Appendix A)

$$\mathcal{H}_{\rm HFI} = A_{\rm hf}(\boldsymbol{J}\cdot\boldsymbol{I}), \tag{1.11}$$

where

$$\begin{aligned} A_{\rm hf} &= A_J + A_{\rm core} \\ &= 2\mu_{\rm B}\gamma_{\rm N}\hbar\langle r^{-3}\rangle\langle J\|N\|J\rangle + A_c(g_J - 1) \end{aligned} \tag{1.12}$$

In eq. (1.12), the first and the second terms are the hyperfine coupling constant due to the orbital and the core polarization, respectively. The hyperfine field $H_{\rm hf}$ is then expressed as a sum of the orbital term and the core polarization term:

$$\boldsymbol{H}_{\rm hf} = \boldsymbol{H}_J + \boldsymbol{H}_{\rm core}, \tag{1.13}$$

where

$$\boldsymbol{H}_J = \frac{A_J}{\gamma_{\rm N}\hbar g_J\mu_{\rm B}}(-g_J\mu_{\rm B}\boldsymbol{J}), \tag{1.14}$$

$$\boldsymbol{H}_{\rm core} = \frac{A_c}{\gamma_{\rm N}\hbar g_J\mu_{\rm B}}(g_J - 1)(-g_J\mu_{\rm B}\boldsymbol{J}). \tag{1.15}$$

In these formula we find that the hyperfine interaction is parallel to the orbital magnetic moment, $\boldsymbol{\mu}_J = -g_J\mu_{\rm B}\boldsymbol{J}$. Since the orbital hyperfine field in eq.(1.14) is usually dominant to the rare earth and actinide nucleus, the Knight shift is given by

$$K(T) \simeq \frac{\langle H_J^z\rangle}{H_0} = \frac{A_J}{g_J\mu_{\rm B}}\frac{\langle\mu_J^z\rangle}{H_0} = \frac{A_J}{N_{\rm A}g_J\mu_{\rm B}}\chi_{\rm f}(T), \tag{1.16}$$

where H_0 is the external field along the z-axis and $\chi_{\rm f}$ is the magnetic susceptibility due to f-electrons , respectively. We can not only measure the T-dependence of the Knight shift due to f-electrons but also quantitatively investigate the physical origin of the Knight shift from the hyperfine coupling constant. Similarly, the nuclear spin-lattice relaxation rate is also considered to be due to f-electrons. The magnetic on-site NMR is therefore

Table 1.1: Typical NMR parameter about nuclei

Nucleus	Nuclear spin	Natural abundance (%)	γ_N (MHz/T)	Q (barns)
^{1}H	1/2	99.985	42.5759	–
^{51}V	7/2	99.76	11.19	−0.04
^{63}Cu	3/2	69.09	11.285	−0.16
^{171}Yb	1/2	14.31	7.499	–
^{235}U	7/2	0.72	0.784	4.1

Table 1.2: Examples of the NMR observation in rare earth and actinide series. The P and M represent the paramagnetic state and the magnetically ordered state, respectively. (○): the NMR observation is reported, (−): not reported, and (×): no existence of the stable isotope with a nuclear spin.

	Ce	Pr	Nd	Pm	Sm	Eu	Gd	Tb	Dy	Ho	Er	Tm	Yb
P	×	○	−	×	−	−	−	−	−	−	−	○	○[a]
M	×	○	○	×	○	○	○	○	○	○	○	○	−
	Th	Pa	U	Np	Pu	Am	Cm	Bk	Cf	Es	Fm	Md	No
P	×	×	−	×	×	×	×	×	×	×	×	×	×
M	×	×	○[b]	×	×	×	×	×	×	×	×	×	×

a) Ref.[20] and this work.
b) This work.

quite a powerful method to investigate the f-electronic state in rare earth and actinide compounds.

Now why does the magnetic on-site NMR have seldom been performed for rare earth and actinide compounds ? First is due to a very short relaxation rate, T_1 and T_2, which results from a large hyperfine field and a small characteristic energy, ϵ, in f-electron systems. The relaxation time, $\sim \epsilon/A^2$, is too short to be observed by means of the pulsed NMR technique. Second is due to the properties of rare earth and actinide nucleus. The typical NMR parameter about nuclei is shown in Table 1.1. The proton NMR, frequently utilized for chemical and medical analyses, has the most advantageous condition on observation of the NMR signals; the ^{1}H nucleus has the large nuclear gyromagnetic ratio and the rich natural abundance. In contrast, the ^{235}U nucleus has a very small nuclear gyromagnetic ratio of 0.784 MHz/T and a poor natural abundance of 0.72 %. Comparing with ^{51}V and ^{63}Cu nuclei which play a significant role for the NMR experiments in the solid state physics, the ^{235}U nuclear gyromagnetic ratio is less than 1/10 and the natural abundance is much less. It is therefore very difficult to observe the ^{235}U NMR signal for the sample prepared by the natural uranium under a magnetic field of a few ten T. In addition, the nuclear quadrupole moment of ^{235}U is considerably large. This indicates that the electric nuclear quadrupole interaction is comparable with or larger than the Zeeman term in the Hamiltonian of a nuclear spin under usual magnetic fields. Thus the resonance frequency is widely distributed under the applied field. Examples of the NMR observation for rare earth and actinide series are given in Table 1.2. For most of the rare

earth nuclei the NMR signals are observed only in the magnetically ordered state. This is because the relaxation rate is drastically reduced below the transition temperature. In the antiferromagnetic state, the marked reduction is particularly observed since the energy gap due to anisotropy is present. We thus learn that trial to the NMR observation should be carried out at low temperatures for a system with a energy gap, Δ, such as an antiferromagnet, a superconductor and a Kondo semiconductor. In fact, the ^{171}Yb and ^{235}U NMR signals in the present study are only observed at $T \ll \Delta$.
In summary,

- The NMR quantities give direct informations on f-electrons.
- The hyperfine interaction can be approximately evaluated from a free ion. We thus can discuss quantitatively the NMR quantities.
- Observation of the magnetic rare earth or actinide NMR signal is restricted within a narrow temperature region of a particular material.

1.3 Purpose for the Present Thesis

Almost all NMR studies of f-electron systems have been discussed on the basis of the indirect information obtained by the non-magnetic ligand NMR. Although these studies have contributed considerably to the investigation of the overall qualitative properties in a given material, they do not always have provided us with knowledge about the local f-electronic states. Our goal is to understand anomalous magnetic and electric properties in f-electron systems from the microscopic standpoint.

The purpose for the present study is the observation of rare earth and actinide NMR and the acquisition of typical examples with respect to the magnetic hyperfine interaction and the nuclear electric quadrupole interaction. This will be the starting point of our goal. We have performed trial to observation of the rare earth and actinide NMR and succeed in observation of ^{171}Yb and ^{235}U NMR. Particuraly, the ^{235}U NMR of UO_2 is the first report for actinide NMR in solids, and the hyperfine interaction is important as an example of U^{4+} ions. We also carried out the ^{17}O NMR experiments to investigate the magnetic structure and Jahn-Teller distortion of UO_2. The direction of the magnetic hyperfine field is necessary especially for the evaluation of the nuclear electric quadrupole interaction at the U sites. For our future reference to search for ^{235}U NMR signals and to analyze the ^{235}U NMR results in uranium intermetallics with more complicated electric states, we discuss the hyperfine interaction on the uranium ions through the comparison between the experimental values and the calculated values for a free ion.

Chapter 2

Experimental Technique

2.1 Sample Preparation

A single crystal of YbB_{12} is provided by Prof. F. Iga, Mr. N. Shimizu and Prof. T. Takabatake at the Hiroshima University. Recently, they succeeded for the first time in growing a large single crystal of YbB_{12} (6mm$\phi\times$ 50 mm) by floating zone method using a developed image-furnace with four xenon lamps[8]. We have performed the NMR experiments by using the single crystal sliced in the plane perpendicular to ⟨111⟩ (0.2 ∼ 0.3 mm thickness), because the rf penetration depth is estimated to be about 0.15 mm at 30 K and 100 MHz. In order to get the better S/N ratio, we crushed the sliced crystal into powder. The powdering, however, enlarges the Curie term of susceptibility at low temperatures like Ref. [8], and also broadens the NMR spectra. Thus we use the powder sample only for measurements of $1/T_1$.

Two 93% ^{235}U enriched samples of UO_2 are provided by Mr. S. Tsutsui, Mr. N. Masaki and Dr. A. Nakamura at the Japan Atomic Energy Research Institute (JAERI). One (UO_2#1) was prepared by heating a uranium-oxide at 1273 K under an atmosphere of hydrogen, Another sample (UO_2#2) was made by oxidizing the ^{235}U-metal powder, pulverized into small particles by heating a purified ^{235}U-metal ingot at 673 K under an atmosphere of hydrogen. The x-ray diffraction patterns of both samples were well indexed by the fluorite structure, but the peak near the phase transition (30.5 K) in the magnetic susceptibility of UO_2#2 is clearer than that of UO_2#1, and the Curie term of UO_2#2 at low temperatures is almost not observed. Both samples were made into 7ϕ-pellets by being pressed and sintered under an atmosphere of hydrogen because of the better filling factor resulting in the better S/N ratio of NMR signals and the shorter pulses per power available.

A ^{17}O enriched sample of UO_2 is provided by Mr. N. Masaki Mr. S. Tsutsui and Dr. A. Nakamura at JAERI. The sample was prepared by the similar method as that of UO_2#2. This powdered sample was sealed in a quartz tube of diameter 8ϕ because the NMR experiments are performed at Institute for Solid State Physics (ISSP) outside the control area for radiation.

2.2 Spectrometer

All experiments using the highly enriched uranium were carried out in the control area for radiation at JAERI. Hence, we newly set up the NMR spectrometer or carry on some instruments of Yasuoka's laboratory in the control area at JAERI. A typical block diagram of the NMR spectrometer is displayed in Fig. 2.1. The NMR experiments were almost carried out by using a conventional pulsed phase-coherent spectrometer. For search for signals and measurements of the frequency spectra, a pulsed phase-incoherent spectrometer was also used because of simplification of the experimental conditions. The high-speed averaging function of the digital scope is particuraly utilized in the measurements of relaxation rate. The standard NMR spectra, obtained by sweeping magnetic field at a constant frequency, is measured by recording the output of a boxcar integer instead of the digital scope.

First, radio frequency (rf) pulses are made by mixing a rf continuous wave from a signal generator and a gate pulse from a pulse generator through the double balanced mixer (DBM). Second, the rf pulses with four different phases are made by the 180-hybrid junction and the 90-hybrid junction, and the choice of them can be controlled by the gate pulse from the pulse generator. Particuraly, for the spin-echo measurements with a $\pi/2$-τ-π pulse sequence, alternating the phase is very useful to cancel out the ringing after the π pulse and to subtract background. Next, these rf pulses are amplified up to about a few hundred volts and they cause the rf field, $H_1 \sim 100$ Oe, at the sample position in the pick-up coil of the tank circuit. The small voltage (∼ a few micro volts) in the pick-up coil induced by the nuclear magnetization is detected by using the technique of phase sensitive detection. Finally, the spin-echo signals with a phase information are averaged and analyzed by the digital scope.

The pulse generator, the digital scope and the other several generator can be controlled through GPIB bus or I/O port from the personal computer in which we use the application programmed by the Visual Basic, and the data is transferred through the GPIB bus from the digital scope to the personal computer.

2.3 Spectra Measurements

In the ^{171}Yb and ^{17}O NMR experiments in the paramagnetic state, the spin-echo spectra are obtained by sweeping magnetic field at a constant frequency of ν_0. The external magnetic field was applied using superconducting solenoids, whose maximum fields are approximately 12 T and 9 T. We obtain the Knight shift, K, from the following relation,

$$K = \frac{H_0 - H_{\rm res}}{H_{\rm res}} \times 100 \ \ \%, \tag{2.1}$$

where $H_0 = \nu_0/\gamma_N$, and $H_{\rm res}$ is the field evaluated from the peak position of spectrum; for the ^{171}Yb and the ^{17}O NMR, the gyromagnetic ratios are 7.499 T/MHz and 5.772 T/MHz, respectively, and the NMR spectra are measured at 96.7 MHz for ^{171}Yb NMR and 62.1 MHz for ^{17}O NMR.

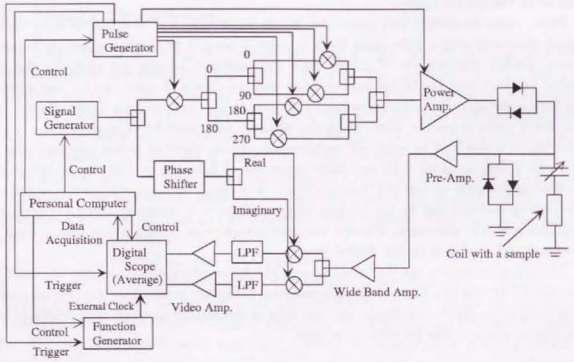

Figure 2.1: A typical block diagram of a pulsed phase-coherent NMR spectrometer. The symbols, $\otimes$, represent the double balanced mixer (DBM).

Searching for ^{235}U resonance signals were performed by using a UO_2#1 sample at zero-field and below 4.2 K. Since the hyperfine field at the U sites is estimated as 270 $\pm$ 20 T from the Mössbauer experiments[21, 22], we concentrically search for the signal at the corresponding frequency between 150 and 250 MHz. The frequency spectrum is obtained by measuring the intensity of spin-echo signal averaged by the digital scope at each frequency.

2.4 T_1 Measurements

The nuclear spin-lattice relaxation rate was measured by the standard saturation (or inversion) recovery technique. The single saturation (or inversion) pulse is applied at a time, t, before the spin-echo sequence and the recovery of nuclear magnetization is obtained by changing the t. The nuclear spin-lattice relaxation rate is determined by fitting the recovery curve, for the ^{171}Yb and ^{17}O NMR, to the single exponential function [Fig. 2.2]

$$\frac{M(\infty) - M(t)}{M(\infty)} = M_0[\exp(-\frac{t}{T_1})], \tag{2.2}$$

and for ^{235}U NMR, to the following function for the magnetic relaxation process [Fig. 2.3]

$$\frac{M(\infty) - M(t)}{M(\infty)} = M_0[A\exp(-\frac{t}{T_1}) + B\exp(-\frac{6t}{T_1}) + C\exp(-\frac{15t}{T_1}) + D\exp(-\frac{28t}{T_1})]. \tag{2.3}$$

Here $M(t)$ and $M(\infty)$ are the nuclear magnetization at time t after the saturation (or inversion) pulse, and that at the thermal equilibrium state, respectively. In the eq. (2.3), A, B, C, D and M_0 are equal to 1/84, 3/44, 75/364, 1225/1716 and 1, respectively, if the initial condition is such that the central transition is completely saturated and the populations of the other spin levels are unaffected. The recovery curve can be fitted more reasonably for the UO_2#2 sample although the no significant difference between these samples is observed for the resonance frequencies.

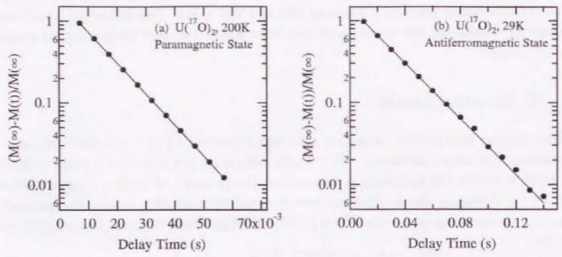

Figure 2.2: Typical recovery curves of spin-echo intensity in the ^{17} O NMR of UO_2. (a) in the paramagnetic state and (b) in the antiferromagnetic state.

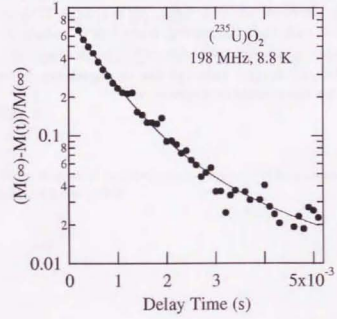

Figure 2.3: A typical recovery curve of spin-echo intensity in the ^{235} U NMR of UO_2.

Chapter 3

Experimental Results and Analyses

3.1 Kondo Semiconductor, YbB_{12} — ^{171}Yb NMR

In general, the Knight shift at the rare earth sites has quite a large amplitude due to the orbital hyperfine coupling constant, and thus one needs to search for NMR signals at the field of $\nu_0/(1+K)\gamma_N$ rather than the usual resonance condition, ν_0/γ_N. Since the hyperfine coupling constant of a free Yb^{3+} ion is simply estimated as 115 T/μ_B (See Chapter 4 and Appendix. A), we obtain the resonance field for a constant frequency by using the hyperfine coupling constant and the magnetic susceptibility. Near the magnetic field estimated for a constant frequency of 96.7 MHz, we observed a spin-echo signal below 10 K for the sliced single crystal of YbB_{12}. As seen in Fig. 3.1, the spin-echo spectrum has a T-dependence, and the spin-echo signal is drastically weaker as T increases. We can thus exclude that the signal is attributed to nonmagnetic materials around the coil other than YbB_{12}. The T-dependence of the Knight shift is shown in Fig. 3.2 (a). The hyperfine coupling constant is estimated to be 115 T/μ_B at 10 K from the measured Knight shift, 66.44 %, and the susceptibility, 3.219 $\times 10^{-3}$ emu/mol. There is therefore no longer doubt for the ^{171}Yb spin-echo signal in YbB_{12}. In spite of experiments within the narrow temperature range, the direct observation for the magnetic on-site nucleus gives the clear evidence for the physical origin of magnetic susceptibility; the susceptibility of YbB_{12} remained at $T \to 0$ is due to the orbital contribution of Yb^{3+} ions.

The T-dependence of $1/T_1$ is shown in Fig. 3.2 (b). The relaxation rate drastically increases as T increases, and the energy gap, Δ, is roughly evaluated as $\sim$100K. This is comparable to the energy gap obtained by other experiments[7, 23, 24]. The most interesting feature is that unlike the $1/T_1$ at the ^{11}B sites, the upturn in the T-dependence of $1/T_1$ is not observed below 15 K[7]. If we estimate the $^{11}(1/T_1)$ from the relation, $(^{11}\gamma_N\ ^{11}A)^2/(^{171}\gamma_N\ ^{171}A)^2 \times ^{171}(1/T_1)$, by using the ^{11}B hyperfine coupling constant, 0.65 kOe/μ_B, and the value of $^{171}(1/T_1)$ at 10 K, we obtain 1.4×10^{-3} s^{-1}, which is smaller than the observed value, 0.2 s^{-1}. This suggests that the extra contribution is mainly dominant to the ^{11}B relaxation rate at low temperatures. Since the ^{11}B relaxation rate is much smaller than the ^{171}Yb one, the relaxation processes associated with the magnetic impurities may be more exaggeratedly detected at low temperatures.

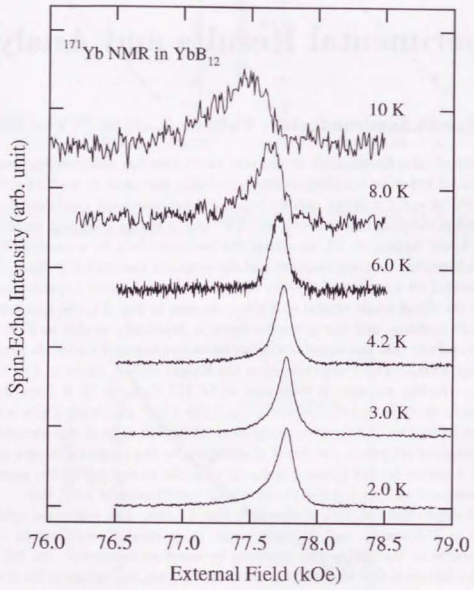

Figure 3.1: The ^{171}Yb Spin-Echo Spectrum in a single crystal of YbB_{12}.

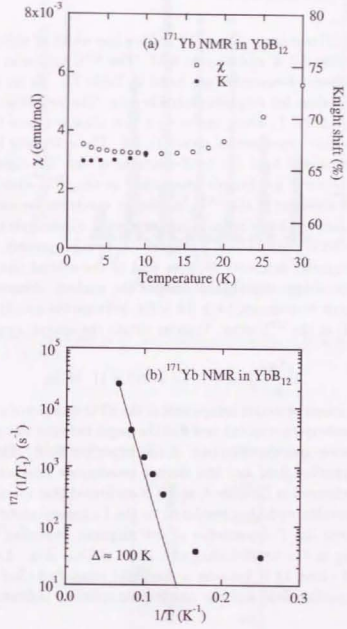

Figure 3.2: Temperature dependences of (a) the Knight shifts and (b) the spin-lattice relaxation rates in ^{171}Yb NMR of YbB_{12}. (a) The external field is parallel to ⟨111⟩ for a sliced single crystal. (b) For the powder sample crushed the sliced single crystal.

3.2 Antiferromagnet, UO_2 — ^{235}U and ^{17}O NMR

3.2.1 ^{235}U NMR

Seven $^{235}U(I = 7/2)$ resonance lines with a sharp line width of about 1 MHz have been observed in UO_2 below 4.2 K and at zero field. The ^{235}U spin-echo spectrum is shown in Fig. 3.3. All resonance frequencies are listed in Table 3.1. As far as we know, this is the first NMR observation for magnetic actinide ions. The hyperfine field at the U sites is evaluated as 252.3 ± 0.5 T, which agrees with that obtained from the ^{238}U Mössbauer experiments within their experimental errors[21, 22]. The extremely large hyperfine field is considered as the orbital field due to 5f-electrons of the $^3H_4$ state. Most interesting feature is that the electric quadrupole interaction at the ^{235}U sites is clearly observed although it was not observed in the ^{238}U Mössbauer spectrum because of the inherently poor resolution. In rare earth and actinide ions an electric quadrupole interaction normally exists even in the cubic crystalline field if magnetic ordering is present, because the spatial alignment of the magnetic moments requires that of the orbital momentum and causes an axially symmetric charge distribution around the nucleus. Almost equal separations between the resonance frequencies, 14 ± 0.4 MHz, indicate the axially symmetric electric field gradient (EFG) at the ^{235}U sites. Thus we obtain the electric quadrupole interaction as follows,

$$|\frac{e^2qQ}{h}(3\cos^2\theta - 1)| = 392 \pm 11 \ \text{MHz}, \tag{3.1}$$

where eq is the maximum principal component of the EFG tensor evaluated at the nucleus, Q is the nuclear quadrupole moment and θ is the angle between the principal axis of the maximum EFG tensor and the direction of the hyperfine field. The detailed analyses of the magnetic hyperfine field and the electric quadrupole interaction produced by f-electrons will be performed in Chapter 4, and it is confirmed that the observed quadrupole interaction is comparable with that produced by the Γ_5-ground state of U^{4+}.

We have measured the T-dependence of the magnetic hyperfine field, H_{hf}, and the quadrupole splitting in the antiferromagnetic state of UO_2 [Fig. 3.4 (a)]. The signals cannot be observed above 14 K because of too short relaxation time. No T-dependence of the magnetic hyperfine field and the quadrupole splitting indicates no change of the

Table 3.1: Resonance frequencies of ^{235}U $(I = 7/2)$ NMR in the antiferromagnetic state of UO_2

Quadrupole splitting (I_z)	Resonance Frequency (MHz)
$\pm 5/2 \leftrightarrow \pm 7/2$	155.6, 240.3
$\pm 3/2 \leftrightarrow \pm 5/2$	169.6, 226.0
$\pm 1/2 \leftrightarrow \pm 3/2$	183.7, 211.9
$-1/2 \leftrightarrow +1/2$	197.8

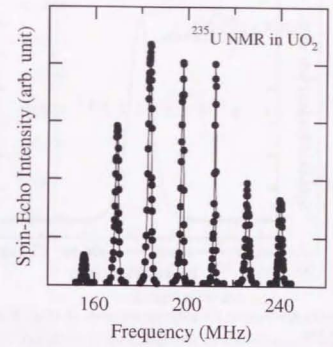

Figure 3.3: ^{235}U spin-echo spectrum in the antiferromagnetic state of UO_2 at 1.5 K. The resonance frequencies are given in Table 3.1.

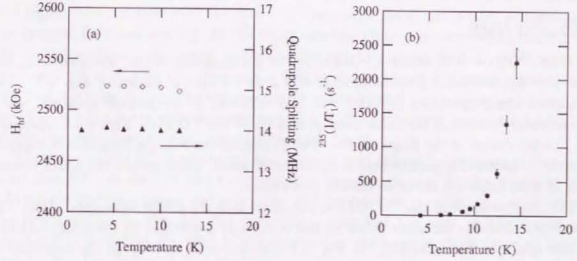

Figure 3.4: (a) Temperature dependence of the hyperfine field and Quadrupole splitting at the ^{235}U sites. (b) Temperature dependence of the ^{238}U nuclear spin-lattice relaxation rate.

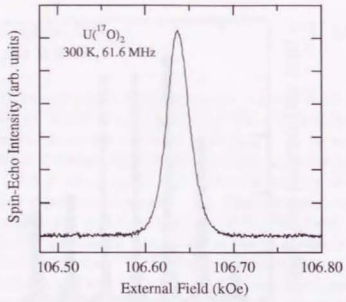

Figure 3.5: ^{17}O spin-echo spectrum in the paramagnetic state of UO_2. It is measured on the pulse condition of 4.2 μs-τ-8.4μs.

distribution of 5f-electrons around the nucleus at low temperatures, and is consistent with that of the ordered moment by the neutron scattering experiments.

Figure 3.4 (b) shows the T-dependence of the ^{235}U nuclear spin-lattice relaxation rate, which indicates a T^7-like behavior rather than the activation type (also see Fig. 3.14). The spin wave excitation in UO_2 will be discussed in Sec. 3.2.3.

3.2.2 ^{17}O NMR

The ^{17}O(I = 5/2) NMR spectrum in the paramagnetic state, obtained from the spin-echo signal with a pulse condition of 4.2 μs-τ-8.4μs, is shown in Fig. 3.5. The symmetric sharp spectrum (FWHM$\simeq$ 30 Oe) indicates no quadrupole splitting, which can be understood from the cubic point symmetry at the ^{17}O sites. Figure 3.6 represents the T-dependences of the Knight shifts. The T-independence of the Knight shift suggests that the transferred hyperfine field is significantly small, which means the direct overlap with 5f-wave functions are of secondary importance.

The interest result in the ^{17}O NMR experiments is in the antiferromagnetic state. The spectrum drastically broadens below T_N and is strongly dependent on the pulse condition for the spin-echo formation[25]. In Fig. 3.7, the spin-echo spectra on the condition of 1.4 μs-τ-2.8μs are shown for several time intervals, τ, at 28 K. As seen in Fig. 3.9, this anomalous τ-dependence of the spin-echo spectra is attributed to the modulation of the spin-echo decay of which the period is dependent on the resonance field. Thus we cannot measure the exact spin-echo intensity unless the time intervals are enough long to such

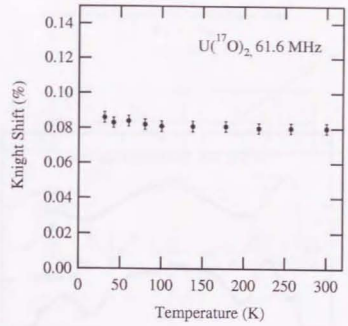

Figure 3.6: Temperature dependence of the Knight shift for the ^{17}O sites in the paramagnetic state.

an extent that the modulation effects is negligible. In fact, the spectrum for $\tau = 1000\mu$s is similar to the powder pattern spectrum in the antiferromagnetic state at the sites of which internal field, $H_{\rm int}$, is smaller than the external field, $H_{\rm ext}$[26]. For the purpose to illustrate the powder pattern spectrum in the antiferromagnetic state, we demonstrate the ideal spectrum at $H_{\rm ext} \gg H_{\rm int}$ in Fig. 3.8. The NMR signals at the edges on the lower and higher field side arise from the sites with the internal fields antiparallel and parallel to the external field, respectively. As the result, the line width is corresponding to $2H_{\rm int}$ and the spectrum shows a symmetric feature for the usual resonance field, $H_0 = \nu_0/\gamma_N$. From the line width in Fig. 3.7 (e), the internal field at the oxygen sites is roughly estimated to be about 6.5 kOe. An unexpected spectrum is also obtained on the same pulse condition as 4.2 μs-τ-8.4μs in the paramagnetic state[Fig. 3.10(b)]. The two resonance fields, $H^{\pm}_{\rm ma}$, in this spin-echo spectrum are almost symmetric for H_0.

These anomalous NMR results can be explained very well by the presence of the axially symmetric EFG at the ^{17}O sites in the antiferromagnetic state as follows. The first-order quadrupole splitting causes the spin-echo modulation with a period, $\tau_{\rm m}$, equivalent to the splitting[27]. In Fig. 3.9, the modulation period at the edge on the spectrum is about a half period at H_0, that is, the splitting at the edge is about twice as large as that at H_0. This indicates that the direction of internal field is parallel to the principal axis of the maximum EFG tensor (Z-axis) from the character of the first-order quadrupole splitting[28]. In Fig. 3.9 (a) and (b), the higher harmonic terms with the period of $\tau_{\rm m}/2$ are also observed. These terms are attributed to the excitation condition where the rf pulses

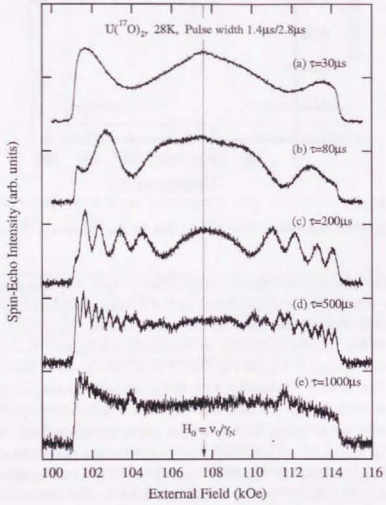

Figure 3.7: ^{17}O spin-echo spectrum in the antiferromagnetic state of UO_2 at 62.1 MHz for various time intervals between $\pi/2$ and π pulse. The dotted line represents the position of $H_0 = \nu_0/\gamma_N$. The spectrum (e) is similar to the typical powder pattern spectrum in the antiferromagnetic state.

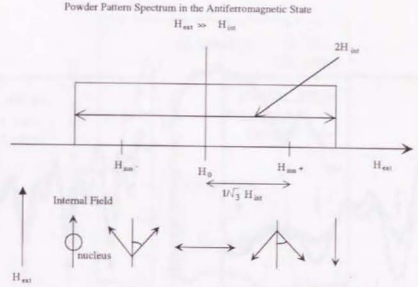

Figure 3.8: Demonstration of the powder pattern spectrum in the antiferromagnetic state at $H_{\rm ext} \gg H_{\rm int}$. The NMR signals at the edges on the lower and higher field side arise from the sites with the internal fields antiparallel and parallel to the external field, respectively. The resonance fields, $H^{\pm}_{\rm ma}$, on the magic angle condition are also shown in the case that the direction of the internal field is parallel to the Z-axis.

excite only a single line but also multiple lines splitted by the nuclear electric quadrupole interaction[27]. In this case, the shape of spin-echo decay is strongly dependent on the pulse condition but the period of modulation is not affected. In Fig. 3.9 (a) and (b), we confirm no change in the period from the spin-echo decay on the pulse condition of 14μs-τ-28μs or 18μs-τ-36μs suppressing the amplitude of rf field. Furthermore, no modulation at the two resonance fields, $H^{\pm}_{\rm ma}$, is observed [Fig. 3.9 (c)]. This indicates that these resonances are on the magic angle condition with $\theta = \cos^{-1}(1/\sqrt{3}) \equiv \alpha$ in which the first-order quadrupole splitting vanishes. Here, θ is the angle between the Z-axis and the external field. This magic angle condition is also supported by the result that the difference between $H^{\pm}_{\rm ma}$ and H_0 is about $1/\sqrt{3}$ times as large as the half width of the spectrum in Fig. 3.7(e). The reason why the two lines are only observed on the pulse condition of 4.2 μs-τ-8.4μs can be explained by the quadrupole splitting. The effective rf field for the central transition ($1/2 \leftrightarrow -1/2$ of I=5/2) splitted by the nuclear electric quadrupole interaction is three times as large as that for the transition in the absence of the quadrupole splitting[28]. Since the pulse width tipping the magnetization is inversely proportional to the amplitude of rf field, the exciting pulse width for the central transition is 1/3 of that for the transition in the absence of the quadrupole splitting. The spectrum on the magic angle condition is therefore obtained only on the same pulse condition as 4.2 μs-τ-8.4μs in the paramagnetic state without the quadrupole splitting. As a result,

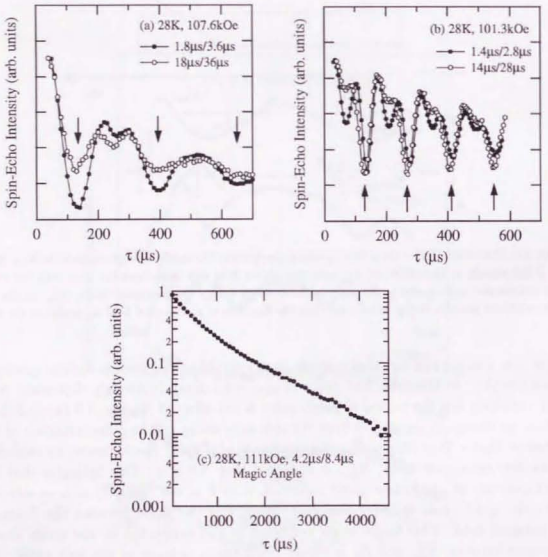

Figure 3.9: ^{17}O spin echo decay curve. (a): at an edge on the lower field side in the spectrum of Fiq. 3.7 (e). (b): at the resonance field, $H_0 = \nu_0/\gamma_N$. (c): at the peak in Fig. 3.10 (b). The arrows in (a) and (b) represent the minimum of spin-echo modulation corresponding to the quadrapole splitting. The higher harmonic terms with a half of that is also observed even on the pulse condition of $14\mu s$-τ-$28\mu s$ or $18\mu s$-τ-$36\mu s$. The asymmetric feature of the modulation is strongly dependent on the pulse condition but the period is not affected.

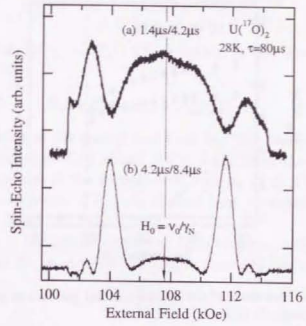

Figure 3.10: ^{17}O spin-echo spectra on the different pulse conditions. The spectrum (b) is measured on the same pulse condition as $4.2\mu s$-τ-$8.4\mu s$ in the paramagnetic state.

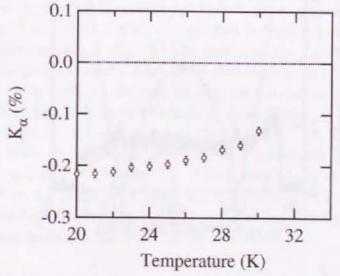

Figure 3.11: Temperature dependence of K_α in the antiferromagnetic state.

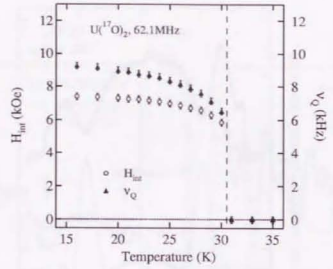

Figure 3.12: Temperature dependence of the internal field and the nuclear quadrupole frequency at the ^{17}O sites in the antiferromagnetic state.

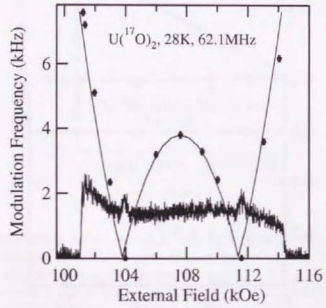

Figure 3.13: Field dependence of the modulation frequency in the spin-echo decay. The solid curve represents calculated one by using H_{int} = 6.59 kOe and ν_Q = 7.6 kHz on the assumption that the modulation is caused by the quadrupole splitting due to the axially symmetric EFG.

we can express $H^{\pm}_{ma}$ as follows,

$$H^{\pm}_{ma} = \frac{H_0 \pm H_{int}\cos\alpha}{1+K_\alpha} = \frac{H_0 \pm \frac{1}{\sqrt{3}}H_{int}}{1+K_\alpha}, \tag{3.2}$$

where $K_\alpha = (H_0 \pm (1/\sqrt{3})H_{int} - H^{\pm}_{ma})/H^{\pm}_{ma}$ is defined as the shift at the angle α. This can be also rewritten by

$$K_\alpha = H_0/((H^{-}_{ma} + H^{+}_{ma})/2) - 1, \tag{3.3}$$

which represents the shift of the central field from H_0. We determined the K_α from the $H^{\pm}_{ma}$ and the T-dependence of K_α is shown in Fig. 3.11. Using the value of K_α and $H^{\pm}_{ma}$, we obtain the T-dependence of the internal field from eq. (3.2) [Fig. 3.12]. Although we do not know the physical origin of K_α, the internal field is insensitive to the small value of K_α as found in eq. (3.2).

On the assumption of the axially symmetric EFG tensor and $H_{int}//Z$-axis, the modulation frequency due to the quadrupole splitting is expressed by,

$$\nu_m(\theta) = |\frac{\nu_Q}{2}(3\cos^2\theta - 1)|, \tag{3.4}$$

where the angle θ can be written by

$$\cos\theta = (H_0 - H_{res})/H_{int}. \tag{3.5}$$

In these formula, ν_m and ν_Q are the modulation frequency and the electric quadrupole frequency, respectively, and H_{res} is the external field at which the resonance is observed. The solid curve in Fig. 3.13 represents the one calculated by substituting H_{int} = 6.59 kOe and ν_Q = 7.6 kHz at 28 K into eq. (3.4) and (3.5). The presence of the axially symmetric EFG at the oxygen sites is reconfirmed by this good agreement with the measured frequencies in Fig. 3.13. Here, the ν_Q is evaluated by multiplying a factor 2 from the modulation frequency at $H_{res} = H_0$. We also measured the T-dependence of ν_Q, which obviously shows the presence of the Jahn-Teller distortion at the antiferromagnetic transition temperature [Fig. 3.12]. In the next section, we will discuss the magnetic structure and Jahn-Teller distortion of UO_2 on the basis of these results.

The nuclear spin-lattice relaxation rate at the ^{17}O sites, $^{17}(1/T_1)$, is measured in the antiferromagnetic state to investigate the spin wave excitation. The T-dependence of $^{17}(1/T_1)$ is shown in Fig. 3.14. As seen Fig. 2.2(b), even in the antiferromagnetic state, the recovery curve on the magic angle condition is fitted very well to a single exponential function. The relaxation rate remarkably reduces below T_N, and shows a T^7-like behavior at low temperatures similar to the result of the ^{235}U NMR.

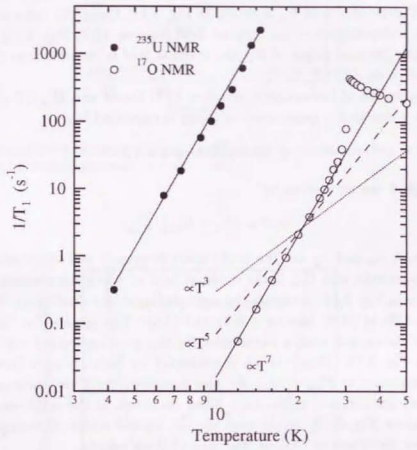

Figure 3.14: Temperature dependence of $(1/T_1)$ in the antiferromagnetic state. The open and closed circles represent the relaxation rates for ^{235}U and ^{17}O nuclei, respectively.

3.2.3 Discussion on UO_2

Magnetic Ordering and Jahn-Teller Distortion of UO_2

As denoted in Sec.1.1, it is proposed by the neutron scattering experiments that the magnetic structure of UO_2 is a multi-$\boldsymbol{k}$ structure, $2\boldsymbol{k}$- or $3\boldsymbol{k}$-structure with a distortion of the oxygen atoms from the equilibrium position. Also in this study, the Jahn-Teller distortion is clearly observed below T_N from the presence of the EFG at the ^{17}O sites. In this section, we discuss the multi-$\boldsymbol{k}$ structure of UO_2 from the ^{17}O NMR results. Our results are as follows,

(1) $H_{int} = 7.4 \pm 0.2$ kOe below 16 K.

(2) $\nu_Q = 9.3 \pm 0.2$ kHz below 16 K.

(3) The internal field is parallel to the Z-axis; $H_{int}//V_{ZZ}$.

(4) The EFG tensor at the ^{17}O sites is uniaxial; $V_{YY} = V_{XX}$, that is, $\eta = 0$

where (X,Y,Z) is the principal axis of the EFG tensor, V, at the ^{17}O sites and the asymmetric parameter, η, is defined as $(V_{YY} - V_{XX})/V_{ZZ}$. The parameter, η, is useful to represent the asymmetric character of the EFG tensor and it has a value from 0 (axially symmetric EFG) to 1. In Fig. 1.10, the $3\boldsymbol{k}$-structure has a threefold rotation axis at each oxygen site while the distortion in the $2\boldsymbol{k}$-structure is orthorhombic. In the consideration of the symmetry of lattice distortion, the observed axially symmetric EFG tensor indicates that the $3\boldsymbol{k}$-structure is realized. In order to verify the possibility of the $3\boldsymbol{k}$-structure in more detail, we calculated the classical dipole field and the EFG tensor due to lattice charges.

First, the classical dipole field at the oxygen atoms is given by

$$\langle \mathbf{H}^i_{dip} \rangle = \sum_j 3 \frac{\langle \mu_j \rangle \cdot \mathbf{r}_{ij}}{r^5_{ij}} - \frac{\langle \mu_j \rangle}{r^3_{ij}}, \tag{3.6}$$

where $\langle \mu_j \rangle$ is the time average of the electronic spin moment at the jth atom, which is at a distance $\mathbf{r}_{ij}$ from the ith atom. The dipole field is calculated by the summation over 20 unit cells for each case of the $2\boldsymbol{k}$- and $3\boldsymbol{k}$-structure in Fig. 1.10. Here, we neglect the distortion of the oxygen atoms because the small displacement of 0.014 Å do not affect magnitude and direction of the internal field. Using the ordered moment, $1.74\mu_B$, the dipole fields at the oxygen sites are estimated to be about 4.2 kOe for both structures, which is of the same order as the experimental value. The direction of the dipole field represents in Fig. 3.15(a) and (b). For the $2\boldsymbol{k}$-structure, the dipole fields at the oxygen sites point along the $\langle 101 \rangle$ directions of the cubic unit cell whereas for the $3\boldsymbol{k}$-structure these point along the $\langle 111 \rangle$ directions.

Next, we calculated the EFG tensor at the oxygen sites for the $2\boldsymbol{k}$- and the $3\boldsymbol{k}$-structures on the point charge approximation. For the oxygen ions in which all electron shells are closed, the contribution of the EFG is considered to be mainly due to the surrounding lattice charges. Since the oxygen sites have the cubic point symmetry in the paramagnetic state, the finite electric quadrupole interaction in the antiferromagnetic

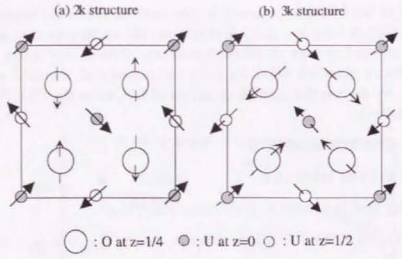

Figure 3.15: The (001) projections of the fluorite structure for the $2\boldsymbol{k}$- and the $3\boldsymbol{k}$-structures. The dipole fields at the oxygen atoms point along the $\langle 101 \rangle$ directions for the $2\boldsymbol{k}$-structure and along the $\langle 111 \rangle$ directions for the $3\boldsymbol{k}$-structure.

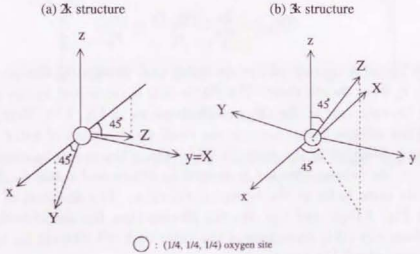

Figure 3.16: The principal axis of the EFG tensor (the XYZ frame) at a (1/4, 1/4, 1/4) oxygen site. The (x,y,z) frame is taken for the cubic crystalline axis.

state indicates the presence of the lattice distortion from the cubic symmetry. The EFG tensor, $V_{\rm mn}$, produced by an ion of charge Ze at $\mathbf{r}$ can be written by,

$$V_{\rm mn} = \frac{Ze(3r_{\rm m}r_{\rm n} - r^2\delta_{\rm mn})}{r^5}, \tag{3.7}$$

where m and n represent x, y or z-axis along the cubic axes. The EFG tensor is calculated from the summation over the 20 unit cells. We determine the principal axis of the EFG tensor by diagonalizing the calculated one. When the principal component of the EFG tensor is defined as $|V_{\rm ZZ}| \geq |V_{\rm YY}| \geq |V_{\rm XX}|$, we get for the (1/4,1/4,1/4) oxygen site with a displacement of 0.014 Å in the $2\boldsymbol{k}$-structure,

$$\begin{aligned} V_{\rm XX} &= -0.09 \times 10^{12} \text{ esu} \quad // \ (0,1,0), \\ V_{\rm YY} &= -9.18 \times 10^{12} \text{ esu} \quad // \ (1,0,-1), \\ V_{\rm ZZ} &= 9.27 \times 10^{12} \text{ esu} \quad // \ (-1,0,-1), \end{aligned} \tag{3.8}$$

and in the $3\boldsymbol{k}$-structure,

$$\begin{aligned} V_{\rm XX} &= -5.36 \times 10^{12} \text{ esu} \quad // \ (-2,1,1), \\ V_{\rm YY} &= -5.36 \times 10^{12} \text{ esu} \quad // \ (0.226,-0.792,0.566), \\ V_{\rm ZZ} &= 10.72 \times 10^{12} \text{ esu} \quad // \ (1,1,1). \end{aligned} \tag{3.9}$$

Here, we neglect the EFG produced by charges of the oxygen sites because it is of order of 10^9 esu. As seen in Fig. 3.16, the Z-axes at the (1/4,1/4,1/4) oxygen site for the $2\boldsymbol{k}$-and the $3\boldsymbol{k}$-structure are the $(\bar{1}0\bar{1})$ and the (111) direction, respectively. In the same way, we can calculate the EFG tensors for all eight oxygen sites equivalent to (1/4,1/4,1/4) and (1/4, 1/4, -1/4). The Z-axes for these oxygen sites occupy all four $\langle 101 \rangle$ directions for the $2\boldsymbol{k}$-structure and all eight $\langle 111 \rangle$ directions for the $3\boldsymbol{k}$-structure. In the exact evaluation of the EFG tensor, one needs to consider the contribution arising from the closed shells which become distorted under the influence of the nonspherical EFG. This contribution is usually expressed in term of the Sternheimer antishielding factor, γ_∞[29], which is of order of unity. The EFG tensor can therefore be written by $V_{\rm ZZ}(1-\gamma_\infty)$. In this analysis, however, we neglect the antishielding effect because it does not affect the determination of the principal axis of the EFG tensor. Then, the quadrupole frequency and the asymmetric parameter for the $2\boldsymbol{k}$-structure are evaluated to be

$$\begin{aligned} \nu_Q &= 2.6 \text{ kHz} \quad (Z // H_{\rm dip}), \\ \eta &\simeq 1, \end{aligned} \tag{3.10}$$

and for the $3\boldsymbol{k}$-structure,

$$\begin{aligned} \nu_Q &= 3.0 \text{ kHz} \quad (Z // H_{\rm dip}), \\ \eta &= 0, \end{aligned} \tag{3.11}$$

where we use -2.6 $\times 10^{-2}$ barn as the nuclear quadrupole moment of ^{17}O nucleus. For both multi-$\boldsymbol{k}$ structures, the Z-axis is parallel to the dipole field, which is satisfied with

the experimental result (3). The calculated EFG which is of the same order as the experimental value (result (2)) indicates that the contribution due to lattice charges is dominant. The most important result is that the asymmetric parameter for the $2\boldsymbol{k}$-structure is just opposite to the result (4) while one for the $3\boldsymbol{k}$-structure agrees with the result (4). The $2\boldsymbol{k}$-structure is therefore excluded and the $3\boldsymbol{k}$-structure is the most likely of the multi-$\boldsymbol{k}$ structures.

Spin Wave Excitation in the Antiferromagnetic State

Interacting with nuclear spins as a result of hyperfine coupling, the spin waves (or magnons) can be scattering by the nuclear spins, as well as absorbed and emitted by them; finally, spin waves can be converted into lattice vibrations (phonons). Thus, the relaxation process caused by fluctuating local field at the nucleus gives us important knowledge on the spin wave excitation. Direct processes, in which the nuclear spin is flipped and a spin wave is absorbed or emitted, are usually unimportant because of restriction on energy conservation. However, Raman processes, in which the nuclear spin flip arises from the absorption of a spin wave of energy $\hbar\omega_k$ and the simultaneous emission of another spin wave of energy $\hbar\omega_{k'}$, as $|\hbar\omega_k - \hbar\omega_{k'}|$ is equal to the nuclear Zeeman energy, can be a major contribution in the relaxation process. The T-dependence of $1/T_1$ due to two-magnon processes is expressed by [32],

$$\frac{1}{T_1} \propto T^3 \qquad \text{for } T \gg T_{AE}, \tag{3.12}$$

$$\frac{1}{T_1} \propto T^2 \exp(-T/T_{\mathrm{AE}}) \quad \text{for } T \ll T_{\mathrm{AE}}, \tag{3.13}$$

where $k_{\mathrm{B}}T_{\mathrm{AE}}$ is the initial gap in the spin wave spectrum. For $T \ll T_{\mathrm{AE}}$, we can see the pronounced effect of the energy gap $k_{\mathrm{B}}T_{\mathrm{AE}}$. This character at $T \ll T_{\mathrm{AE}}$ is also expected for processes with the participation of three or more magnons. In fact, the nuclear spin-lattice relaxation rate due to Raman processes is quantitatively confirmed from the ^{19}F NMR in MnF_2[30]. In UO_2, however, the T-dependence of $1/T_1$ between 4.2 and 25 K shows a T^7-like behavior over six orders of the magnitude. Since the energy gap T_{AE} is estimated as about 43 K from the spin wave spectrum in Fig. 1.11, more pronounced reduction of $1/T_1$ is expected if relaxation processes involving only pure magnon excitations are dominant. Then we notice that the quasi-phonon branch observed in Fig. 1.11 has no gap in the dispersion, $E \sim |\mathbf{k}|$. In general, the relaxation process due to phonon excitations is dominant only for the quadrupole relaxation which arises from the interaction between the nuclear quadrupole moments and fluctuations in the EFG at the sites. In the case of UO_2, the quadrupole relaxation due to pure phonon excitations is unexpected because the recovery curve at the ^{235}U sites in Fig. 2.3 means the magnetic relaxation processes. It is known that the coupling between spin wave and phonon modes mixes spin wave character into the phonons and thereby allows the phonons to induce magnetic processes directly. This quasi-phonon branch will be particularly important for magnetic relaxation process at $T \ll T_{\mathrm{AE}}$. The relaxation rate

due to the Raman processes of the mixed magnon-phonon modes is given as $1/T_1 \propto T^7$ for $T \ll T_{\mathrm{AE}}$[31], which agrees with the experimental result. Unfortunately, we cannot quantitatively discuss the relaxation rate because it includes an unknown parameter with respect to the magnon-phonon coupling. Considering the first-order phase transition in UO_2 through the strong spin-lattice interaction, it seems to be a reasonable result that the relaxation process through the strong magnon-phonon coupling is dominant at low temperatures.

Chapter 4

Hyperfine Interaction on Rare Earth and Actinide ions

4.1 ^{171}Yb NMR of YbB_{12}

Yb^{3+}: J =7/2, L=3, S=1/2

Magnetic hyperfine interaction

From eq. (1.16) we can evaluate the value of $A_{\rm hf}$ by using $K = 66.44$ % and $\chi = 3.219 \times 10^{-3}$ emu/mol at 10 K:

$$\frac{A_{\rm hf}}{g_J} = 115 \pm 2 \ {\rm T}/\mu_{\rm B}. \tag{4.1}$$

This value of the hyperfine coupling constant is comparable with that obtained by the ^{171}Yb NMR of $YbAl_2$ and $YbAl_3$[20]. In Table 4.1, we show the calculated hyperfine coupling constant for the $J = 7/2$ ground state and the $J = 5/2$ first-excited state of a free Yb^{3+} ion. The values of $H_J^{\rm orb}$ and $H_J^{\rm sC}$ are calculated from the orbital contribution and the spin-dipole contribution in eq. (A.10), respectively. An excellent agreement with the experimental value indicates that the admixture of the $J = 5/2$ first-excited state to the ground state, the core polarization effect and the other fine effects (as the relativistic effect) are very small. We therefore conclude that in the Kondo semiconductor, YbB_{12}, the susceptibility with a finite magnitude at $T \ll \Delta$ is obviously due to the orbital contribution of Yb^{3+}ions. As is well known, a second order in J_z like the Van Vleck susceptibility is also reflected in the Knight shift by the same formula with eq. (1.16) through the hyperfine coupling constant A_J[36]. The susceptibility of YbB_{12} shows a drastic reduction due to the energy gap at the Fermi level and has a character of the nonmagnetic ground state at low temperatures. Hence, the Knight shift may be ascribed to the Van Vleck term as is independent on the density of states at the Fermi level.

Almost all Ce-based Kondo semiconductors also show the large susceptibilities even at $T \ll \Delta$ as seen in Fig. 1.6. Particuraly, for CeNiSn with the orthorhombic structure, the considerably large anisotropy of susceptibility suggests the importance of the orbital contribution[35]. Although the susceptibility of the Kondo semiconductors remained at

low temperatures is believed to be due to the orbital one like the Van Vleck term, we have never confirm it experimentally. This result of the magnetic on-site NMR is therefore a significant evidence.

Table 4.1: Hyperfine coupling constant of a free Yb^{3+} ion calculated by using a nonrelativistic (NREL) Hatree-Fock value of $\langle r^{-3} \rangle = 13.83$ a.u. The values of $H_J^{\rm orb}$ and $H_J^{\rm sC}$ are calculated from the orbital and the spin-dipole contributions in eq. (A.10), respectively.

	$H_J^{\rm orb}$ (T)	$H_J^{\rm sC}$ (T)	H_J (T)	$H_{\rm core}$ (T)	$A_{\rm hf}/g_J$ (T/$\mu_{\rm B}$)
NREL calculation (J=7/2)	519.4	−57.7	461.7	$\simeq 0^{a)}$	115.4
NREL calculation (J=5/2)			593.5	–	207.7
Experiment	–	–	–	–	115 ± 2 (YbB_{12})$^{b)}$
	–	–	–	–	110 ± 10 ($YbAl_2$)$^{c)}$
	–	–	–	–	120 ± 10 ($YbAl_3$)$^{c)}$

a) From unrestricted Hartree-Fock calculations[33, 34].
b) This work.
c) From ^{171}Yb NMR measurements in Ref. [20].

4.2 ^{235}U NMR of UO_2

U^{4+}: J=4, L=5, S=1

Magnetic hyperfine interaction

Since the magnetic hyperfine interaction is independent on the sub-space of the $^3H_4$ ground state due to crystalline field, we obtain

$$\frac{A_{\rm hf}}{g_J} = 145 \pm 2 \ {\rm T}/\mu_{\rm B}, \tag{4.2}$$

where we use the hyperfine field, 253.2± 0.5 T, and the ordered magnetic moment, 1.74 ± 0.02 $\mu_{\rm B}$[14]. Fortunately, for actinide series, the relativistic correction of $\langle r^{-3} \rangle$ is calculated by using a relativistic equivalent of the Slater-modified Hartree-Fock method[38] (Table 4.2). We thus calculated the hyperfine coupling constants, A_J/g_J, for a free U^{4+} ion on the basis of the nonrelativistic and relativistic theory. These results are summarized in Table 4.3. The hyperfine coupling constant of a free U^{3+} ion is also shown as reference. We find that the nonrelativistic calculation gives comparable results with the values of $\langle r^{-3} \rangle$ including relativistic corrections but somewhat cause an overestimation of the hyperfine coupling constant. Comparing between the experimental value and the calculated values of A_J/g_J, the orbital hyperfine field is a major contribution for uranium ions.

For the actinide series, no theoretical calculations have been performed for the core polarization. Dunlap *et al.*, however, have evaluated the core polarization fields from the Mössbauer experiments for some actinide ions[39, 40], and concluded that the core polarization fields are substantially large for the actinide series than for the rare earth series. Assuming that a quantities χ in eq. (A.16) is constant for all actinide ions like the

Table 4.2: The calculated values of $\langle r^{-3} \rangle$ for a free uranium ion on the basis of the relativistic (REL) theory[38].

	$\langle r_l^{-3} \rangle$ a.u.	$\langle r_{sC}^{-3} \rangle$ a.u.	$\langle r_s^{-3} \rangle$ a.u.
U^{4+}	6.164	7.105	−0.431
U^{3+}	5.513	6.469	−0.442

Table 4.3: Hyperfine coupling constants of a free uranium ion. In the nonrelativistic (NREL) estimation, we use $\langle r^{-3} \rangle = 7.82$ a.u for a free U^{4+} ion and $\langle r^{-3} \rangle = 7.24$ a.u for a free U^{3+} ion [37]. In the relativistic (REL) estimation, each contribution of the hyperfine field is calculated from eq. (A.8) by using the values of $\langle r^{-3} \rangle$ in Table 4.2. The values of $H_{\rm core}$ are estimated from the experimental results of Pu^0, Pu^{3+}, Am^0 and Am^{2+} Mössbauer measurements[39, 40], assuming that a quantities χ in eq. (A.16) is constant for all 5f-elements.

	$H_J^{\rm orb}$ (T)	H_J^{sC} (T)	H_J^s (T)	H_J (T)	A_J/g_J (T/μ_B)	$H_{\rm core}$ (T)	$A_{\rm hf}/g_J$ (T/μ_B)
NREL calculation							
U^{4+}	472	44	–	516	161	∼ 48[a)]	∼ 176
U^{3+}	460	16	–	476	164	∼ 74[a)]	∼ 168
REL calculation							
U^{4+}	370.4	41.2	4	415.6	129.9	∼ 48[a)]	∼ 145
U^{3+}	395	14	6.8	415.8	127.1	∼ 74[a)]	∼ 150
Experiment (U^{4+})	–	–	–	–	–	–	145 ± 2 (UO_2)[b)]

a) From the Mössbauer measurements in Ref. [39, 40].
b) This work.

case for 3d and 4d ions, we can roughly estimate the value of $H_{\rm core}$ for the uranium ions as shown in Table 4.3. The important point is that the core polarization fields of actinides give the plus sign unlike 3d or 4d-transition metal series. It is therefore possible that the difference between the experimental value and the calculated orbital term is attributed to the core polarization field.

Nuclear electric quadrupole interaction

In general, the maximum component of the EFG is the sum of several contributions. For UO_2, we can write

$$eq = eq_{5f}(1 - R_{5f}) + eq_{\rm lattice}(1 - \gamma_\infty) + eq'. \tag{4.3}$$

The first term on the right-hand side of eq. (4.3) represents the contribution of the EFG produced by 5f-electrons and R_{5f} is the Sternheimer factor[29] which describes the modification of the EFG by the inner electrons. The second term represents the contribution from the lattice charges and γ_∞ is the corresponding Sternheimer factor. In UO_2, this arises from the lattice distortion below T_N as discussed in Sec. 3.2.3. From the point charge approximation in the $3\boldsymbol{k}$-structure, the electric quadrupole frequency is estimated

Table 4.4: The maximum components of the EFG produced by the 5f-electrons with the pure $^3H_4$ state and the Γ_5-state in the cubic crystalline field, which are calculated from eqs. (A.21) and (A.23). For the Γ_5 states, we calculate them by taking ⟨001⟩ and ⟨111⟩ as axis of quantization.

	eq_{5f} $\times 10^{15}$ (esu/cm^3)
Pure $^3H_4$ state	11.19
Γ_5 ⟨001⟩	1.701
Γ_5 ⟨111⟩	2.765

as 0.6 MHz, which is two orders of magnitude lower than the observed value. The last term gives the EFG from the bonding orbitals if the 5f-electrons participate in bonding. The small transferred hyperfine field at the oxygen sites indicates that the participation in bonding of the 5f-electrons is negligible, and thus we can here consider only the first term.

As seen in Table 4.4, the EFG produced by the pure Hund's rule state is considerably reduced by crystalline field. Here, we use the numerical value of the radial $\langle r_q^{-3} \rangle = 6.249$ a.u. including the relativistic corrections[38, 39]. Since the ground state of UO_2 is the Γ_5 triplet and the magnetic moment is parallel to ⟨111⟩ in the $3\boldsymbol{k}$-structure, we calculated the EFG by using the ground state in eq. (A.25). Then, using the Sternheimer factor 0.35 ± 0.1[42], we obtain the nuclear electric quadrupole interaction,

$$\frac{e^2 q_{5f} Q}{h}(1 - R_{5f}) = 534 \pm 82 \text{ MHz}, \tag{4.4}$$

which is of the same order as the observed nuclear electric quadrupole interaction of 192 MHz for $\theta = 0$ or 396 MHz for $\theta = \pi/2$ in eq. (3.1). Hence, the EFG produced by the 5f-electrons is a major contribution at the ^{235}U sites.

It is very important to determine the principal axis of the EFG tensor, because the ordered quadrupole moment of the Γ_5 state may be characterized. We, however, cannot obtain the angle θ from the above analyses on the basis of the pure Γ_5 triplet. Allen has pointed out that the three levels of the Γ_5 triplet are mixed by an effective quadrupole-quadrupole interaction, which arises from the interaction between the quadrupole moment of the Γ_5 state and the EFG produced by the lattice distortion[16]. More detailed studies in the consideration of the quadrupole-quadrupole interaction in the $3\boldsymbol{k}$-structure will be needed.

Chapter 5

Conclusion

In the present thesis, we have provided with the results of ^{171}Yb NMR in Ytterbium dodecaborides, and ^{235}U and ^{17}O NMR in uranium dioxides, focusing on the application of the magnetic on-site NMR in f-electron systems. In the following, each main conclusion is presented.

^{171}Yb NMR in YbB_{12}

Since only a few examples are reported on ^{171}Yb NMR, the present result will be one of important examples. The success of observation of ^{171}Yb NMR is due to the long relaxation time in the system with an energy gap, Δ, and the high quality single crystal. Because of the large hyperfine field, it is possible that the NMR spectrum is considerably broadened by a little magnetic inhomogeneity in the sample. The high quality sample will be thus important for observation of rare earth and actinide NMR. Unlike the ^{235}U NMR, the enriched sample does not need to be prepared for the ^{171}Yb NMR. The observation of the ^{171}Yb NMR will be, however, restricted within the Kondo semiconductors or the comparatively "light" heavy fermion systems in which the relaxation time should be moderately long.

In the Kondo semiconductor, YbB_{12}, we obtained the considerably large ^{171}Yb Knight shift (66.44 %) at 10 K. The hyperfine coupling constant agrees with the orbital one calculated for a free Yb^{3+} ion. It is therefore concluded that the susceptibility remained at $T \ll \Delta$ arises from the orbital moment of Yb^{3+} (J=7/2) ions. This result is characteristic of the magnetic on-site NMR with the direct information.

^{235}U NMR in UO_2

In a long history of NMR techniques, the actinide NMR has never been observed in solids. Particuraly, for uranium compounds which show various interesting phenomena like non-BCS superconducting states, non-Fermi liquid and quadrupole ordering, the uranium NMR has been strongly requested to investigate the local f-electronic state. As the first step, we succeed in the observation of ^{235}U NMR in UO_2. The important factors for the observation are that we made use of the large hyperfine field and the long relaxation

time in the antiferromagnetic state and that we prepared a 93% ^{235}U-enriched sample. This means that we can observe the ^{235}U NMR by selecting an appropriate material and using the ^{235}U-enriched sample although the nuclear magnetic moment is considerably small and the relaxation time is usually too short. The ^{235}U NMR experiments can therefore be a powerful method for studies of the antiferromagnetic state, the superconducting state or the coexsistent state in uranium intermetallics.

We obtained the magnetic hyperfine interaction and the nuclear electric quadrupole interaction produced by the 5f-electrons, and confirmed that these can be successfully estimated from the numerical value of $\langle r^{-3} \rangle$ for a free U^{4+} ion. As a result, also for the actinide sites, the magnetic hyperfine field almost arises from the orbital magnetic moment.

Unfortunately, the calculated orbital hyperfine field for U^{4+} is comparable with that for U^{3+}, and thus it will be difficult to investigate valence of a uranium ion from the magnetic hyperfine interaction. Alternatively, the nuclear electric quadrupole interaction is expected to be very sensitive to the 5f-electronic states, and may be utilized for vertification of the theoritically proposed ground state although we do not know how much the interaction is modificated for the itenerant 5f-electrons. Any way, we need more examples of the hyperfine interaction at the uranium sites in ionic and metallic uranium compounds.

^{17}O NMR in UO_2

In the antiferromagnetic state of UO_2, we obtain quite characteristic ^{17}O NMR results, which can be explained very well by the presence of the quadrupole splitting due to the axcially symmetric EFG at the oxygen sites. In this study, the application of the spin-echo mudulation for investigation of the EFG is especially a unique example. As a result, we conclude that the $3\boldsymbol{k}$-structure is most likely of the magnetic structures proposed by the neutron scattering experiments. The Jahn-Teller distortion at the antiferromagnetic transition temperature is also clearly observed. In addition, the T-dependence of $1/T_1$ in the antiferromagnetic state supports the presence of the quasi-phonon branch due to the strong magnon-phonon coupling measured by Cowley and Dolling[15].

Appendix A

Hyperfine interaction

The detail discussion on the hyperfine interaction is particularly described in Ref. [43]. In this appendix, we briefly denote the hyperfine interaction within the J-manifold.

In general, the hyperfine interaction for a free ion is expressed by

$$\mathcal{H}_{\rm HFI} = 2\mu_{\rm B}\gamma_{\rm N}\hbar \boldsymbol{I}\cdot[\sum_{\rm k}\{\frac{\boldsymbol{l}_{\rm k}}{r_{\rm k}^3}+(3\cdot\frac{\boldsymbol{r}_{\rm k}(\boldsymbol{s}_{\rm k}\cdot\boldsymbol{r}_{\rm k})}{r_{\rm k}^5}-\frac{\boldsymbol{s}_{\rm k}}{r_{\rm k}^3})+\frac{8\pi}{3}\boldsymbol{s}_{\rm k}\delta(\boldsymbol{r}_{\rm k})\}] \tag{A.1}$$

where $r_{\rm k}$ is distance between the nucleus and the k-th electron with the orbital momentum $\hbar\boldsymbol{l}_{\rm k}$ and the spin momentum $\hbar\boldsymbol{s}_{\rm k}$, and $\gamma_{\rm N}$ is a nuclear gyromagnetic ratio and $\mu_{\rm B}$ is the Bohr magneton. The first term and the second term in eq. (A.1) represent the orbital and spin-dipole contribution from the non s-electrons, respectively, and the last term is the Fermi contact term due to the s-electrons. In LS-coupling $\sum_{\rm i}\boldsymbol{l}_{\rm i}=\boldsymbol{L}$ and $\sum_{\rm i}\boldsymbol{s}_{\rm i}=\boldsymbol{S}$, the magnetic hyperfine interaction can then be written

$$\begin{aligned}\mathcal{H}_{\rm HFI} &= 2\mu_{\rm B}\gamma_{\rm N}\hbar[\langle r_l^{-3}\rangle(\boldsymbol{L}\cdot\boldsymbol{I})+\langle r_s^{-3}\rangle(\boldsymbol{S}\cdot\boldsymbol{I})\\ &+ \langle r_{sC}^{-3}\rangle\xi\{L(L+1)(\boldsymbol{I}\cdot\boldsymbol{S})-\frac{3}{2}\{(\boldsymbol{L}\cdot\boldsymbol{I})(\boldsymbol{L}\cdot\boldsymbol{S})-(\boldsymbol{L}\cdot\boldsymbol{S})(\boldsymbol{L}\cdot\boldsymbol{I})\}].\end{aligned} \tag{A.2}$$

In this formula we use the following relation for the (L,S) term obeying Hund's rule:

$$\sum_{\rm k}\frac{3(\boldsymbol{I}\cdot\boldsymbol{r}_{\rm k})(\boldsymbol{s}_{\rm k}\cdot\boldsymbol{r}_{\rm k})-r_{\rm k}^2(\boldsymbol{I}\cdot\boldsymbol{s}_{\rm k})}{r_{\rm k}^5}=\xi\langle r_{sC}^{-3}\rangle\{L(L+1)(\boldsymbol{I}\cdot\boldsymbol{S})-\frac{3}{2}\{(\boldsymbol{L}\cdot\boldsymbol{I})(\boldsymbol{L}\cdot\boldsymbol{S})-(\boldsymbol{L}\cdot\boldsymbol{S})(\boldsymbol{L}\cdot\boldsymbol{I})\}\}, \tag{A.3}$$

where

$$\xi=\frac{2l+1-4S}{S(2l-1)(2l+3)(2L-1)}. \tag{A.4}$$

In eq. (A.2), $\langle r_l^{-3}\rangle$ and $\langle r_{sC}^{-3}\rangle$ are the averaged distances for the orbital and the spin-dipole hyperfine interaction, respectively. It is often convenient to eliminate the factor $(8\pi/3)$ of the last term in eq.(A.1) by introducing a parameter of $\langle r_s^{-3}\rangle$, because the relativistic effect can be expressed the same $\boldsymbol{I}\cdot\boldsymbol{s}$ form as the Fermi contact term. In a rare earth or actinide ion where J is a good quantum number, we must project the operators $\boldsymbol{L},\boldsymbol{S}$ onto $\boldsymbol{J}$ to find the hyperfine operator for a manifold of states of given J. For this purpose

we replace $\boldsymbol{L}$ by a vector collinear with $\boldsymbol{J}$,

$$\frac{(\boldsymbol{L}\cdot\boldsymbol{J})}{J(J+1)}\boldsymbol{J} \tag{A.5}$$

and similarly $\boldsymbol{S}$ by a vector collinear with $\boldsymbol{J}$,

$$\frac{(\boldsymbol{S}\cdot\boldsymbol{J})}{J(J+1)}\boldsymbol{J}, \tag{A.6}$$

where

$$\begin{aligned}(\boldsymbol{L}\cdot\boldsymbol{J}) &= \frac{1}{2}\{J(J+1)+L(L+1)-S(S+1)\},\\ (\boldsymbol{S}\cdot\boldsymbol{J}) &= \frac{1}{2}\{J(J+1)+S(S+1)-L(L+1)\},\\ (\boldsymbol{L}\cdot\boldsymbol{S}) &= \frac{1}{2}\{J(J+1)-L(L+1)-S(S+1)\}.\end{aligned} \tag{A.7}$$

Thus we have within the J-manifold

$$\begin{aligned}\mathcal{H}_{\rm HFI} &= 2\mu_{\rm B}\gamma_{\rm N}\hbar\frac{1}{J(J+1)}[\langle r_l^{-3}\rangle(\boldsymbol{L}\cdot\boldsymbol{J})+\langle r_s^{-3}\rangle(\boldsymbol{S}\cdot\boldsymbol{J})\\ &+ \langle r_{sC}^{-3}\rangle\xi\{L(L+1)(\boldsymbol{S}\cdot\boldsymbol{J})-3(\boldsymbol{L}\cdot\boldsymbol{J})(\boldsymbol{L}\cdot\boldsymbol{S})\}](\boldsymbol{J}\cdot\boldsymbol{I}).\end{aligned} \tag{A.8}$$

When we introduce a vector $\boldsymbol{N}$:

$$\boldsymbol{N}=\sum_{\rm k}\{\boldsymbol{l}_{\rm k}-\boldsymbol{s}_{\rm k}+3\frac{(\boldsymbol{r}_{\rm k}\cdot\boldsymbol{s}_{\rm k})}{r_{\rm k}^2}\boldsymbol{r}_{\rm k}\}, \tag{A.9}$$

we obtain the constant term which is independent on the magnetic quantum number within the J-manifold:

$$\langle J\|N\|J\rangle=\frac{1}{J(J+1)}\{(\boldsymbol{L}\cdot\boldsymbol{J})+\xi L(L+1)(\boldsymbol{S}\cdot\boldsymbol{J})-3\xi(\boldsymbol{L}\cdot\boldsymbol{J})(\boldsymbol{L}\cdot\boldsymbol{S})\}. \tag{A.10}$$

Assuming that $\langle r_l^{-3}\rangle=\langle r_{sC}^{-3}\rangle\equiv\langle r^{-3}\rangle$ and $\langle r_s^{-3}\rangle=0$, we can written eq.(A.8) into a simple form as follows,

$$\mathcal{H}_{\rm HFI}=A_J(\boldsymbol{J}\cdot\boldsymbol{I}), \tag{A.11}$$

where

$$A_J=2\mu_{\rm B}\gamma_{\rm N}\hbar\langle r^{-3}\rangle\langle J\|N\|J\rangle. \tag{A.12}$$

This is equivalent to an interaction,

$$-\gamma_{\rm N}\hbar(\boldsymbol{H}_J\cdot\boldsymbol{I}) \tag{A.13}$$

where

$$\boldsymbol{H}_J=2\mu_{\rm B}\langle r^{-3}\rangle(-\boldsymbol{N})=\frac{A_J}{\gamma_{\rm N}\hbar}(-\boldsymbol{J}). \tag{A.14}$$

The minus sign in eq.(A.14) indicates that $\boldsymbol{H}_J$ is always in the same direction as the orbital magnetic moment, $-g_J\mu_{\rm B}\boldsymbol{J}$.

We often find the other fine effects on the magnetic hyperfine interaction. Standars and Beck have investigated the relativistic effect on the magnetic hyperfine interaction, and they have shown the formula of an effective hyperfine Hamiltonian with relativistic corrections[41] which is $\langle r_l^{-3}\rangle \neq \langle r_{nC}^{-3}\rangle$ and $\langle r_s^{-3}\rangle \neq 0$ in eq. (A.8). In addition, as a result of the Fermi contact interaction due to closed shells polarized by an open external shell, there is core polarization effect. For the transition metal ion, the effect is particularly important. This hyperfine interaction, $A_c(\boldsymbol{S}\cdot\boldsymbol{I})$, represented by a term similar to Fermi contact term, is projected onto J as follows,

$$A_{\rm core} \equiv A_c \frac{(\boldsymbol{S}\cdot\boldsymbol{J})}{J(J+1)}(\boldsymbol{J}\cdot\boldsymbol{I}) = -2\mu_B\gamma_N\hbar(-\frac{2}{3}\chi)(g_J-1)(\boldsymbol{J}\cdot\boldsymbol{I}). \tag{A.15}$$

Here, χ is defined as a quantity on the density of unpaired spins at the nucleus:

$$\chi = \frac{4\pi}{2S}\sum_n\{|\varphi_{n,s}^+(0)|^2 - |\varphi_{n,s}^-(0)|^2\}, \tag{A.16}$$

where $|\varphi_{ns}^+(0)|^2|$ and $|\varphi_{ns}^-(0)|^2$ are the densities for s-electrons with spin up and down at the origin, respectively. For 4f ions n goes from 1 to 5 and for 5f ions it goes from 1 to 6. As a result, the total hyperfine coupling constant, $A_{\rm hf}$, can be expressed by

$$A_{\rm hf} = A_J + A_{\rm core}, \tag{A.17}$$

and, of course, the total hyperfine field, $\boldsymbol{H}_{\rm hf}$, at the rare earth and actinide nucleus can be also given by

$$\boldsymbol{H}_{\rm hf} = \boldsymbol{H}_J + \boldsymbol{H}_{\rm core}. \tag{A.18}$$

It is significant to divide between the core polarization term and the $(\boldsymbol{S}\cdot\boldsymbol{I})$ term including the relativistic effect in eq.(A.2), since the former is due to the exchange interaction between electrons and the latter is due to the purely single-electron effect.

In order to describe a sub-space of the J-manifold splitted by the crystalline field, it is useful to introduce the fictious spin $\tilde{\boldsymbol{S}}$. When the hyperfine tensor has the same principal axes as the g-tensor, the principal values of these tensors are connected by the following relation:

$$\frac{A_x}{g_x} = \frac{A_y}{g_y} = \frac{A_z}{g_z} = \frac{A_{\rm hf}}{g_J}. \tag{A.19}$$

Thus we can obtain the value of A_J from the NMR experiments without any knowledge of the crystalline field.

The nuclear electric quadrupole interaction with a nuclear spin I for a free ion within a given J-manifold can be expressed as

$$\begin{aligned}\mathcal{H}_Q &= -\frac{e^2Q\langle r_q^{-3}\rangle}{4I(2I-1)}\langle J\|\alpha\|J\rangle[\{3J_z^2 - J(J+1)\}\{3I_z^2 - I(I+1)\} \\ &+ 3(J_x^2 - J_y^2)(I_x^2 - I_y^2)],\end{aligned} \tag{A.20}$$

where $\langle J\|\alpha\|J\rangle$ are reduced matrix elements, tabulated by Elliot and Stevens[44], and $\langle r_q^{-3}\rangle$ is the effective radial parameter on the nuclear electric quadrupole interaction. In

this formula, we consider only matrix elements which are diagonal within the electronic states in the sub-space of the J-manifold lifted by the crystalline field. Then, the maximum EFG component, eq, produced by the electrons is given by

$$eq = -e\langle J\|\alpha\|J\rangle\langle r_q^{-3}\rangle\langle\ |3J_z - J(J+1)|\ \rangle, \tag{A.21}$$

and the asymmetric parameter, η, is

$$\eta = \frac{3\langle\ |J_x^2|\ \rangle}{\langle\ |3J_z^2 - J(J+1)|\ \rangle}, \tag{A.22}$$

where $\langle\ |V|\ \rangle$ represents the matrix element of an operator, V, computed for a given electronic state. In the sub-space of the J-manifold with a fictious spin of $\tilde{\boldsymbol{S}}$, we can obtain the similar formula with eq. (A.20). In the case of the Γ_5 triplet for J=4, the eq is given by the following formula with a fictious spin of $\tilde{S}$=1:

$$eq = -e\langle J\|\alpha\|J\rangle\langle r_q^{-3}\rangle\langle\tilde{1}|3\tilde{S}_z^2 - \tilde{S}(\tilde{S}+1)|\tilde{1}\rangle\langle\tilde{1}|3J_z^2 - J(J+1)|\tilde{1}\rangle, \tag{A.23}$$

where taking the C_2 axis of the cube as axis of quantization,

$$|\tilde{1}\rangle = \frac{1}{\sqrt{8}}(\sqrt{7}|J_z=3\rangle - |J_z=-1\rangle), \tag{A.24}$$

and taking the threefold axis of the cube,

$$|\tilde{1}\rangle = \frac{1}{3\sqrt{6}}(|J_z=-2\rangle + 5|J_z=1\rangle - 2\sqrt{7}|J_z=4\rangle). \tag{A.25}$$

The important point is that the nuclear electric quadrupole interaction strongly depends on the electronic state in the crystalline field unlike the magnetic hyperfine interaction.

References

[1] G. Aeppli and Z. Fisk, Comments Cond. Mat. Phys. **16**, 155 (1992).

[2] A. Menth, E. Buehler and T. H. Geballe, Phys. Rev. Lett. **22**, 295 (1969).

[3] M. Kasaya, F. Iga, K. Negishi, S. Nakai and T. Kasuya, J. Magn. Magn. Mat. **31-34**, 437 (1983).

[4] T. Takabatake, Y. Nakazawa and M. Ishikawa, Jpn. J. Appl. Phys. Suppl. **26-30**, 547 (1987).

[5] S. K. Malik and D. T. Adroja, Phys. Rev. B**43**, 6277 (1991).

[6] T. Takabatake, F. Iga, T. Yoshino, Y. Echizen, K. Katoh, K. Kobayashi, M. Higa, N. Shimizu, Y. Bando, G. Nakamoto, H. Fujii, K. Izawa, T. Suzuki, T. Fujita, M. Sera, M. Hiroi, K. Maezawa, S. Mock, H. v. Löhneysen, A. Bückl, K. Neumaier and K. Andres, J. Magn. Magn. Mat. **177-181**, 277 (1998).

[7] M. Kasaya, F. Iga, M. Takigawa and T. Kasuya, J. Magn. Magn. Mat. **47 & 48**, 429 (1985).

[8] F. Iga, N. Shimizu and T. Takabatake, J. Magn. Magn. Mat. **177-181**, 337 (1998).

[9] S. Fõex, J. Phys. Radium **9**, 37 (1938); V. Jaccarino *et.al.* Phys. Rev. **160**, 476 (1967).

[10] H. Kontani and K. Yamada, J. Phys. Soc. Jpn. **65**, 172 (1996).

[11] H. U. Rahman and W. A. Runciman: J. Phys. Chem. Solids **27**, 1833 (1966). H. U. Rahman and W. A. Runciman: J. Phys. Chem. Solids **30**, 2497 (1969). H. U. Rahman: Physica **45**, 511 (1970).

[12] S. Kern, C. K. Loong and G. H. Lander: Phys. Rev. B **32**, 3051 (1985).

[13] B. C. Frazer *et. al.*: Phys. Rev. **140**, A1448 (1965).

[14] J. Faber, Jr. and G. H. Lander, Phys. Rev. B **14**, 1151 (1976).

[15] R. A. Cowley and G. Dolling, Phys. Rev. **167**, 464 (1968).

[16] S. J. Allen: Phys. Rev. **166**, 166 (1968). S. J. Allen: Phys. Rev. **167**, 167 (1968).

[17] J. Rossat-Mignod, G. H. Lander and P. Burlet, *Handbook on the Physics and Chemistry of the Actinides*, ed. A. J. Freeman and G. H. Lander (North-Holland, Amsterdam, 1984) pp. 415

[18] I. E. Dzyaloshinskii, Commun. Phys. **2**, 69 (1977).

[19] T. Moriya, Prog. Theor. Phys. **16**, 641 (1956).

[20] T. Shimizu, M. Takigawa, H. Yasuoka and J. H. Wernick, J. Magn. Magn. Mat. **52**, 187 (1985).

[21] S. L. Ruby, G. M. Kalvius, B. D. Dunlap, G. K. Shenoy, D. Cohen, M. B. Brodsky and D. J. Lam, Phys. Rev. **184**, 374 (1969).

[22] S. Tsutsui, M. Nakata, N. M. Masaki, M. Saeki, S. Nasu, A. Nakamura, Y. Haga, E. Yamamoto and Y. Onuki, Hyperfine Inter. C, in press.

[23] K. Sugiyama, F. Iga, M. Kasaya, T. Kasuya, M. Date, J. Phys. Soc. Jpn. **57**, 3946 (1988).

[24] F. Iga, M. Kasaya and T. Kasuya, J. Magn. Magn. Mat. **76 & 77**, 156 (1988).

[25] E. L. Hahn, Phys. Rev. **80**, 580 (1950).

[26] For example, A. C. Gossard, J. P. Remeika, T. M. Rice, H. Yasuoka, K. Kosuge and S.Kachi, Phys. Rev. B**9**, 1230 (1974).

[27] H. Abe, H. Yasuoka and A. Hirai, J. Phys. Soc. Jpn., **21**, 77 (1966).

[28] A. Abragam, *Principles of Nuclear Magnetism*, (Clarendon, Oxford, 1961).

[29] R. Sternheimer, Phys. Rev. **84**, 244 (1951).

[30] N. Kaplan, R. Loudon, V. Jaccarino, H. J. Guggenheim, D. Beeman, and P. A. Pincus, Phys. Rev. Letters **17**, 357 (1966).

[31] P. Pincus and J. Winter, Phys. Rev. Lett. **7**, 269 (1961).

[32] V. Jaccarino, *Magnetism II*, ed. G. T. Rado and H. Suhl (Academic Press, New York and London 1966) pp.307

[33] R. E. Watson, P. Bagus, and A. J. Freeman, Bull. Amer. Phys. Soc. **13**, 482 (1968).

[34] A. J. Freeman, *Hyperfine Structure and Nuclear Radiations*, ed. E. Matthias and D. A. Shirley (Norh-Holland, Amsterdam, 1968) pp. 427.

[35] T. Takabatake, F. Teshima, H. Fujii, S. Nishigori, T. Suzuki, T. Fujita, Y. Yamaguchi, J. Sakurai and D. Jaccard, Phys. Rev. B**41** 9607 (1990).

[36] A. M. Clogston, V. Jaccarino and Y. Jafet, Phys.Rev **134**, A650 (1964).

[37] C. J. Lenander, Phys. Rev. **130**, 1033 (1963).

[38] W. B. Lewis, J. B. Mann, D. A. Liberman and D. T. Cromer, J. Chem. Phys. **53**, 809 (1970).

[39] B. D. Dunlap, G. M. Kalvius, *The Actinides: Electronic Structure and Related Properties*, ed. A. J. Freeman and J. B. Darby, Jr. (Academic Press, New York, 1974) p.237

[40] N. Edelstein and R. Mehlhorn, Phys. Rev. **B 2**, 1225 (1970).

[41] P. G. H. Standars and J. Beck, Proc. Roy. Soc. London A**289**, 97 (1965).

[42] B. D. Dunlap, G. M. Kalvius and G. K. Shenoy, Phys. Rev. Lett. **26**, 1085 (1971).

[43] A. Abragam and B. Bleaney, *Electric Paramagnetic Resonance of Transition Ions* (Oxford University Press, Oxfod, 1970).

[44] R. J. Elliott and K. W. H. Stevens, Proc. Roy. Soc. London A**218**, 553 (1953).